RISØ

Risø-R-1479(EN)

Satellite information for wind energy applications

Morten Nielsen, Poul Astrup, Charlotte Bay Hasager, Rebecca Barthelmie, Sara Pryor

Risø National Laboratory
Roskilde
Denmark
November 2004

Risø-R Report

Author: Morten Nielsen, Poul Astrup, Charlotte Bay Hasager, Rebecca Barthelmie, Sary Pryor
Title: Satellite information for wind energy applications
Department: Wind Energy Department

Risø-R-1479(EN)
November 2004

Abstract (max. 2000 char.):
An introduction to satellite information relevant for wind energy applications is given. It includes digital elevation model (DEM) data based on satellite observations. The Shuttle Radar Topography Mission (SRTM) is useful for regional scale wind resource studies. Comparison results from complex terrain in Spain and flat terrain in Denmark are found to be acceptable for both sites. Also land cover type information can be retrieved from satellite observations. Land cover type maps have to be combined with roughness data from field observation or literature values. Land cover type maps constitute an aid to map larger regions within shorter time. Field site observations of obstacles and hedges are still necessary. The raster-based map information from DEM and land cover maps can be converted for use in WASP. For offshore locations it is possible to estimate the wind resources based on ocean surface wind data from several types of satellite observations. The RWT software allows an optimal calculation of SAR wind resource statistics. A tab-file with SAR-based observed wind climate (OWC) data can be obtained for 10 m above sea level and used in WASP. RWT uses a footprint averaging technique to obtain data as similar as possible to mast observations. Maximum-likelihood fitting is used to calculate the Weibull A and k parameters from the constrained data set. Satellite SAR wind maps cover the coastal zone from 3 km and offshore with very detailed information of 400 m by 400 m grid resolution. Spatial trends in mean wind, energy density, Weibull A and k and uncertainty values are provided for the area of interest. Satellite scatterometer wind observations have a spatial resolution of 25 km by 25 km. These data typically represent a site further offshore, and the tab-file statistics should be used in WASP combined with topography and roughness information to assess the coastal wind power potential. Scatterometer wind data are observed ~ twice per day, whereas SAR only are obtained 3 to 8 times monthly. The relatively low number of samples and the absolute uncertainty within the maps, ~ 1.3 ms^{-1}, offer wind resource statistics useful only in pre-feasibility studies or in combination with classical offshore observations.

ISSN 0106-2840
ISBN 87-550-3374-1(Internet)

Contract no.:
ESA EOMD 17736/03/I-IW
STVF SAT-WIND
Sagsnr. 2058-03-0006
Group's own reg. no.:
(1130106-1 and 1130308-1)

Sponsorship:
European Space Agency (ESA), Earth Observation Market Development (EOMD) and Danish Research Agency: Danish Technical Research Council

Pages: 56
Figures: 33
Tables: 10
References: 34

Risø National Laboratory
Information Service Department
P.O.Box 49
DK-4000 Roskilde
Denmark
Telephone +45 46774004
bibl@risoe.dk
Fax +45 46774013
www.risoe.dk

Contents

Preface

Earth observing satellites have been viewing and mapping the globe continuously since the early 1970ties. Satellite information has gradually spread to a wide range of users. Today satellite information is of key importance for environmental monitoring, climate studies and weather forecasting.

The current report provides a brief introduction to satellite information relevant for wind energy applications and a detailed description of examples and methodologies developed for applied use. It is an innovative approach to use satellite observations in wind energy application. The challenges are 1) to quantify advantages and limitations, and 2) to develop state-of-the-art software and service for applied use.

Wind resource mapping for land sites and in coastal areas depends upon digital maps of topography and roughness. Maps of topography from the Shuttle Radar Topography Mission (SRTM)[1] are described and compared to classical maps. Roughness mapping based on satellite-derived land cover type maps for which each cover type is assigned relevant roughness lengths is presented and compared to state-of-the-art roughness maps. Software is developed for applied use in the Wind Atlas and Analysis Program (WASP).

Satellite observations provide surface wind vector observations over the ocean (but not over land). Offshore wind resource mapping based on various types of satellite wind observations including scatterometer, altimeter and Synthetic Aperture Radar (SAR) observations is described. Examples and comparison to meteorological observations is presented as well as a description of software for applied use.

1 Listing of acronyms is given in Appendix A

1 Brief introduction to satellite information relevant for wind energy application

Digital elevation model (DEM) data can be obtained from radar interferometry as is the case with the Shuttle Radar Topography Mission (SRTM) during an 11-day mission in 2000 led by the Jet Propulsion Laboratory (JPL) in the USA. Radar observations from two antennas allow a very accurate digital elevation map to be produced for the area on the globe that the sensor covered. This map is available from http://www2.jpl.nasa.gov/srtm/.

Land cover maps typically are retrieved from optical satellite sensors, i.e. instruments that record reflected visual and near-infrared electromagnetic radiation during daylight hours and cloud free conditions. The methodology on mapping land cover types is related to differences between the reflected radiation in various bands such as blue, green, red, and near-infrared as a function of land cover type. The reflected values allow a grouping of pixels[2] into clusters. Most land cover types have a set of unique reflectance characteristics during a seasonal development phase. This is used to assess the type of land cover present in each pixel.

A classical series of multi-spectral optical observations is available from Landsat http://geo.arc.nasa.gov/sge/landsat/. The aim of the Landsat program is to map land cover types and detect changes. These satellite observations provide basis for the CORINE land cover map covering several European countries http://dataservice.eea.eu.int/dataservice/, the National Land Cover data map of the USA http://edcwww.cr.usgs.gov/products/landcover/nlcd.html, the new US map http://www.mrlc.gov/mrlc2k_nlcd.asp and the Danish Areal Information System (AIS) http://ais.dmu.dk among others.

For the entire globe, Landsat images are available in false-colour (three channels) at https://zulu.ssc.nasa.gov/mrsid/ and as sample images (six channels) from http://glcf.umiacs.umd.edu/data/landsat/. High-resolution optical observations are also available from SPOT, IKONOS, QuickBIRD, IRS-1C LISS-III among others and medium-resolution optical observations from NOAA AVHRR, MODIS Terra and Aqua, Envisat MERIS, SeaWIFS among others. Methods on mapping land cover types are well developed in digital satellite processing (Lillesand and Kiefer, 1987).

For wind energy application the major limitation is that not all land cover types are described sufficiently accurate with a single roughness value. This means that field visits will be necessary in order to verify the roughness locally. The advantage may be that much larger regions can be mapped in a shorter time using satellite-based land cover maps.

Ocean surface wind vector mapping from satellites is a relatively new discipline. With the launch of a scatterometer on-board the first European Remote Sensing (ERS-1) satellite, the era began in 1991. Since then a continuous data-series is available. Scatterometers on-board ERS-1, ERS-2, QuikSCAT and Midori are designed to provide ocean wind vectors within nominal limits, typically around ± 2 ms^{-1} and 20º. QuikSCAT currently provides the most frequent global coverage with observations twice per day for most of the globe (missing a little near the equator). The wind vector data typically are

2 pixel is short for picture element

stored as 25 km by 25 km grid cells http://podaac-esip.jpl.nasa.gov/poet/ or 50 km by 50 km http://www.ifremer.fr/cersat/. The archive of QuikSCAT wind maps covers five years. The archive of ERS scatterometer is the longest spanning 13 years and it is available at http://www.argoss.nl/. Scatterometer surface ocean wind data are assimilated to atmospheric and marine models for improved weather forecasting and for use in operational services.

Wind vector data also can be retrieved from satellite Synthetic Aperture Radar (SAR) images. This is a very different set of observations compared to scatterometer wind vector observations. First of all SAR instruments are not developed specifically for surface ocean wind mapping but for sea ice monitoring, vegetation and moisture monitoring (floods), etc. Secondly the observation rate is rather low. For ERS SAR it is ~ 36 images per year for a given location but as the archive already spans 13 years, up to 400 images can be found for some areas but far fewer for others. Therefore it is recommended to check the SAR image availability in the European Space Agency (ESA) archive at http://pooh.esrin.esa.it/services/catalogues.html for any site of interest. So far there is not an archive of SAR-based wind vector maps available.

It is necessary to obtain raw images, calibrate those with freeware available from ESA at http://earth.esa.int/services/best/, and finally apply an empirical wind retrieval algorithm in order to obtain winds. Software for the latter was developed in a EU-research project (WEMSAR, Wind Energy Mapping using SAR) by the Nansen Environmental and Remote Sensing Centre (NERSC) http://www.nersc.no/ and it is currently being refined within the EO-windfarm project, http://www.eo-windfarm.org/. Satellite images from the new European Envisat satellite in orbit since 2002 is being included.

Envisat provides Advanced SAR (ASAR) images. It means that the sensor can be programmed to a number of different configurations. One mode is similar to ERS SAR. ERS SAR images can be calculated into wind maps covering 100 km by 100 km with wind grid cell resolution of 400 m by 400 m. For wind energy a very interesting mode at Envisat is the ASAR Wide Scan Mode (WSM) with a lower spatial resolution ~ 2.5 km by 2.5 km wind grid cells but with a more frequent revisit interval and covering up to 400 km by 400 km. The Canadian Radarsat-1 satellite operating since 1995 also has a wide scan mode option. Examples of wind maps from ERS SAR and QuikSCAT, and an image from Envisat ASAR WSM is given in Appendix B and a list of available satellite data relevant for ocean surface wind mapping is given in Appendix C.

In summary, satellite-based mapping of topography, land cover types and ocean surface winds from scatterometer are well-known technologies within the satellite remote sensing community. The major task is to prepare the data for easy and reliable inclusion for wind engineering application. Satellite SAR wind mapping however is a greater challenge as the methods for wind vector retrieval are less well proven and the technical work open to improvement. Software is developed and now offered within EO-windfarm.

2 Validation of SRTM digital elevation maps

The Shuttle Radar Topography Mission (SRTM) 3-arcsecond resolution digital elevation maps (DEM) have been validated against height contour maps for two areas, a small 9 times 8 km area in Rioja, Spain, and a larger 60 times 118 km area along the west coast of Jutland, Denmark.

Vestas A/S has kindly provided the height contour map of Rioja, while the one of Jutland has been produced at Risø. The SRTM 3-arcsecond maps are provided free of charge by the US Geological Survey, and have been downloaded from their Internet page "ftp://edcsgs9.cr.usgs.gov/pub/data/srtm/Eurasia/".

2.1 Validation procedure

The SRTM data have been projected onto a UTM (Universal Traverse Mercator) 100 m resolution pixel map and equivalent pixel maps have been produced from the height contour maps. The height differences between corresponding pixels have been binned and the so obtained distribution of height differences compared to the goal for the SRTM data.

2.2 Rioja, Spain

The treated Spanish area extends from southwest corner 578000e, 4659000n to northeast corner 587000e, 4667000n, UTM zone 30, datum ED50. A plot of the contour map is seen in figure 1. The SRTM data refer to datum WGS84, and as the difference between ED50 and WGS84 positions are very close to 100 m east-west and 200 m north-south, the SRTM data have been extracted for the area 577900e,

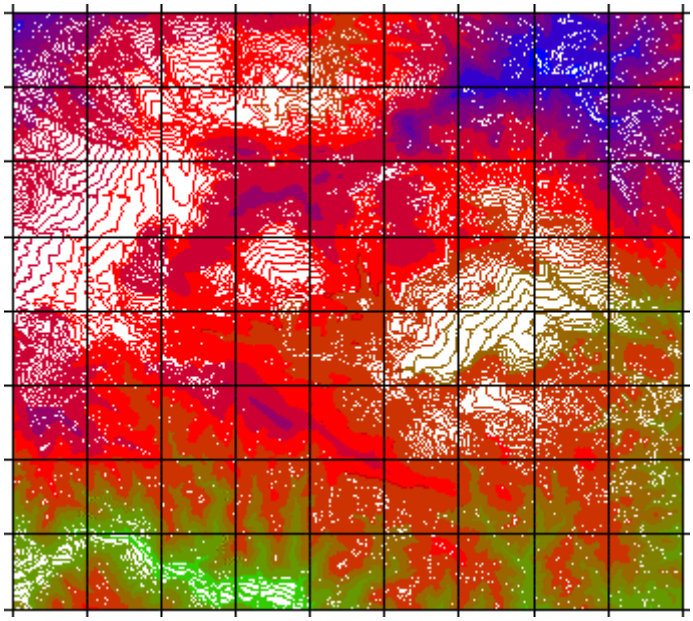

Figure 1. Height contour map of part of Rioja, Spain.

4658800n to 586900e, 4666800n, UTM zone 30, datum WGS84. Figure 2 shows the pixel maps extracted from the contour map and the SRTM maps. The difference is hard to tell by eye. The height differences are shown in figure 3a, and it can be seen that the numerically higher values to some extent follow the contours of the maps, indicating that some positioning error between the two maps may be partly responsible. Binning the

height differences, SRTM minus contour map heights, into 1 m bins and plotting the number of pixels in each bin gives figure 3b. The mean difference is 0.15 m and the standard deviation is 6.9 m.

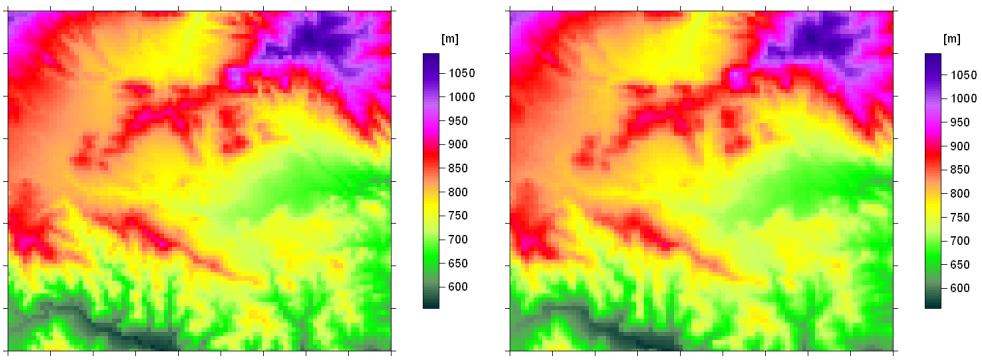

a *b*

Figure 2: 91 times 81 pixel elevation maps [m] from a) the contour map, b) the SRTM maps.

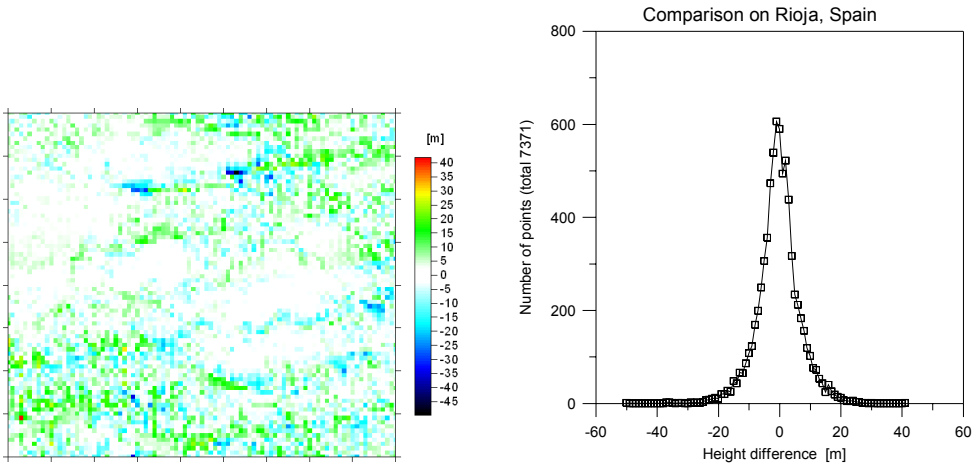

a *b*

Figure 3: SRMT minus contour map height differences: a) map, b) distribution.

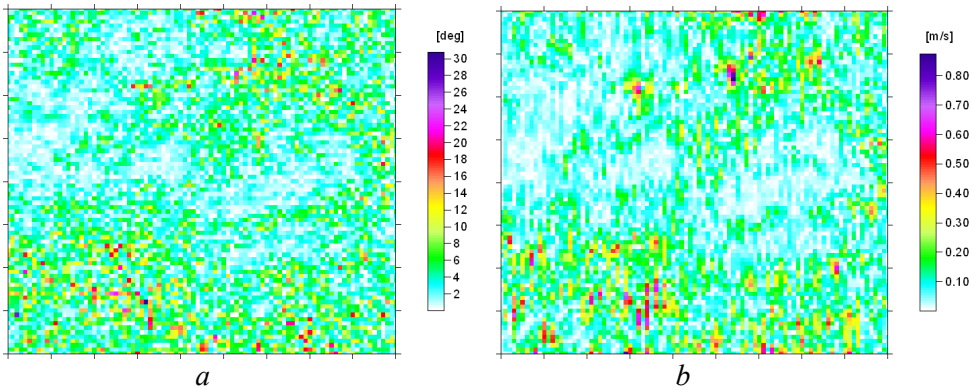

a *b*

Figure 4: a) SRTM minus contour map absolute terrain inclination differences [deg]. b) Absolute wind speed differences, SRTM and contour map based, 100 m above ground, 10 m/s mean wind speed.

2.2.1 Implication on calculated wind

The implication of the height differences on wind resource estimation can be studied by using a model for the flow over the terrain, applying both maps, and calculating the wind speed differences obtained between the two. The flow model available for this purpose, the LINCOM model (Astrup and Larsen 1999), is not really well suited for a terrain as complex as the actual, with slopes of more than 45 degrees. LINCOM is based on linearized equations for perturbations in a mean wind, and assumes the perturbations to be small compared to this mean wind. This assumption gets violated in a too steep terrain, but especially near the ground. At larger heights the winds are influenced less by the ground, and the perturbations are smaller. Applying it 100 m above the actual ground and specifying a mean wind of 10 m/s, strictly west, the wind speed differences obtained with the two maps is anywhere within 0.9 m/s, figure 4b. They correlate with the inclination differences in the flow direction, figure 4a.

2.3 Western Jutland, Denmark

Western Jutland is a relative flat area, with no heights above 100 m, and with gentle sloops not exceeding 10 degrees on a 100 m resolution. The area selected is from southwest corner 439000e, 6102000n to northeast corner 499000e, 6220000n, UTM zone 32, datum WGS84, and the resolution again 100 m. The used contour map and the pixel map produced from this are both shown in figure 5. The SRTM maps covering the area contain voids, i.e. pixels with unknown heights and masked with the value -32768.

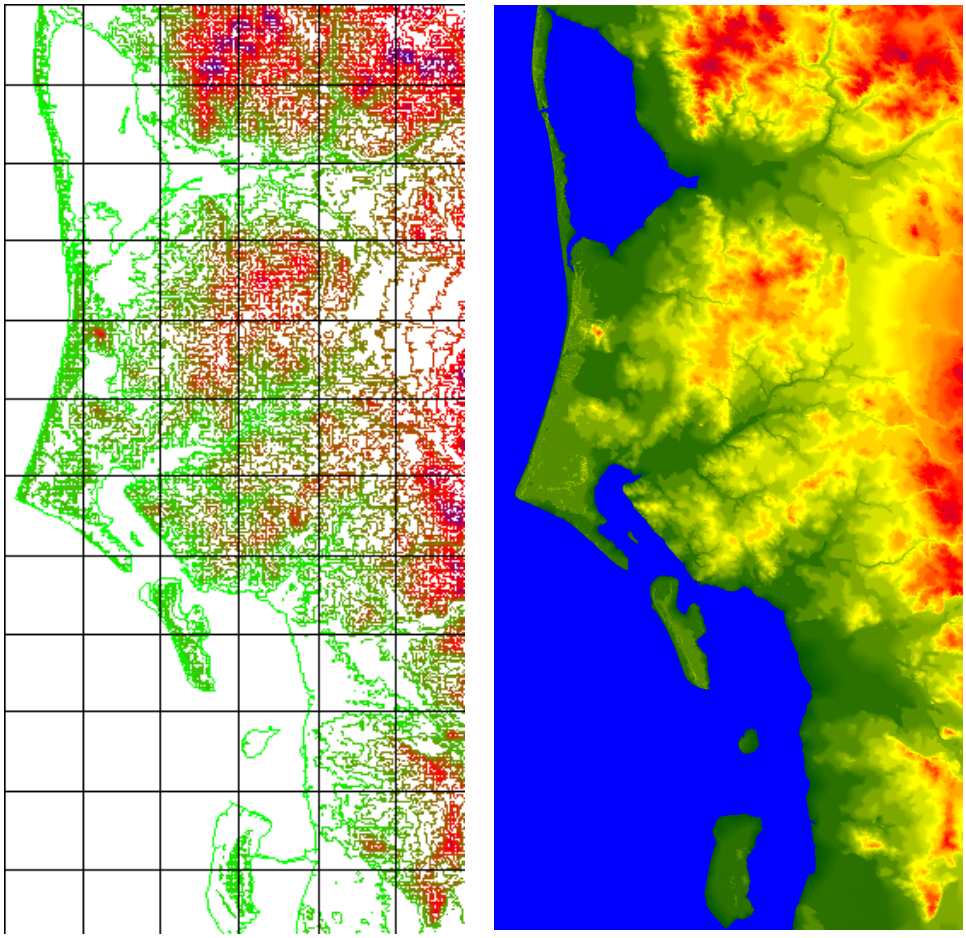

Figure 5: Contour and contour derived pixel height maps of Western Jutland

Within the treated area such voids were only found in the water part of the map. Grid cells with number -32768 were replaced with zero prior to comparison to the contour map. But a little north of the treated area, a small void area was found surrounded by heights around 40 m. This would have been less easy to correct, interpolation being the only option.

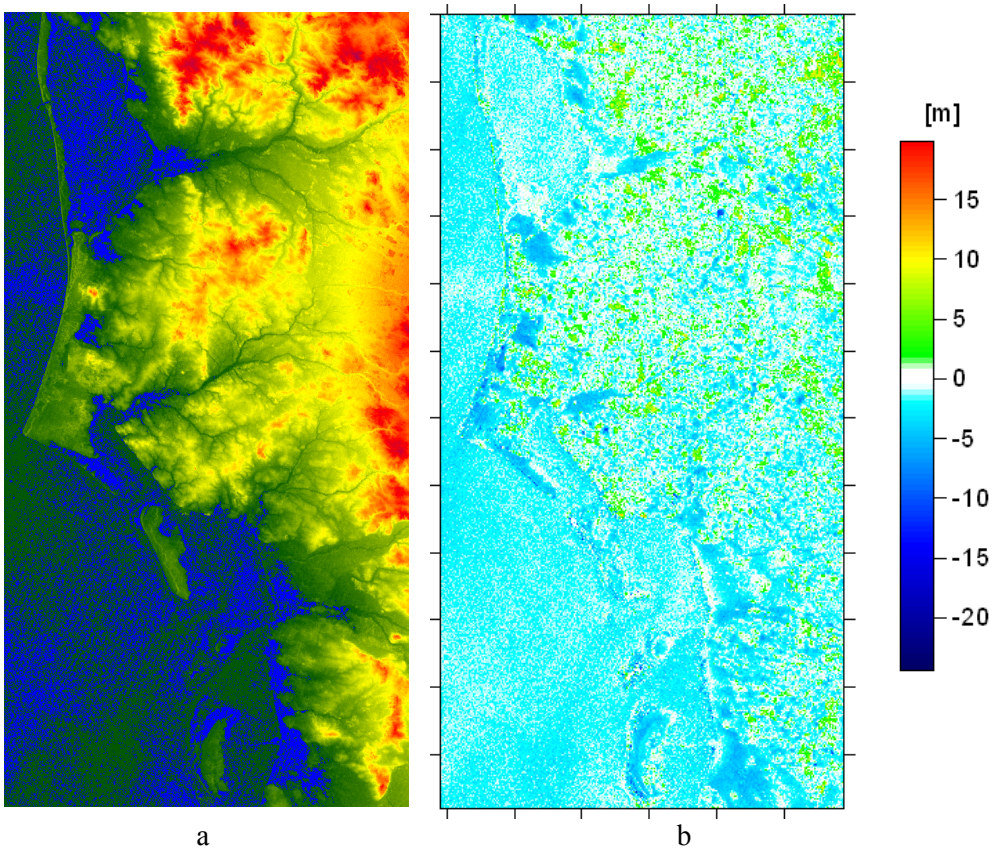

Figure 6: a) SRTM derived pixel map, b) difference between SRTM and contour map. The shown color scale only applies to the difference map.

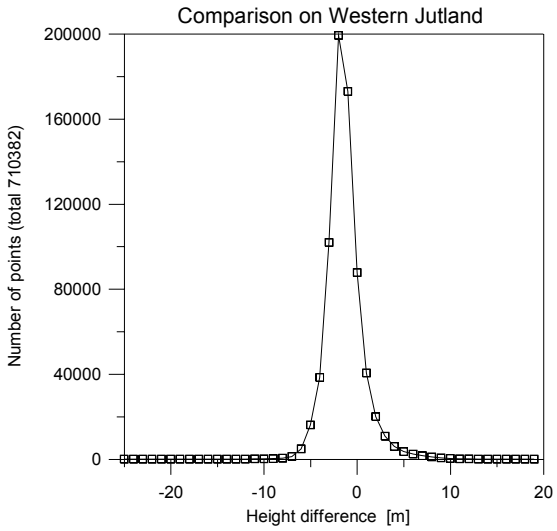

Figure 7: Distribution of height differences, SRTM minus contour map.

There are other pixels with no good values, here e.g. values down to -23 m, but without local knowledge such errors can be hard to spot. In figure 6a the SRTM derived map is shown, but with negative heights replaced by +1 m, and so looking dark green; blue is zero. In figure 6b the difference between the SRTM map and the contour map is shown. It is seen, that the SRTM height of the sea and of much of the land is slightly low while part of the land is somewhat high. Binning the differences and plotting the distribution produces figure 7. The mean difference is -1.7 m, the standard deviation 2.0 m.

2.3.1 Implication on calculated wind

Applying LINCOM with each of the two maps, again specifying strictly westerly 10 m/s mean wind 100 m above ground and calculating the wind speed differences between these two cases, one obtains the map of figure 8.

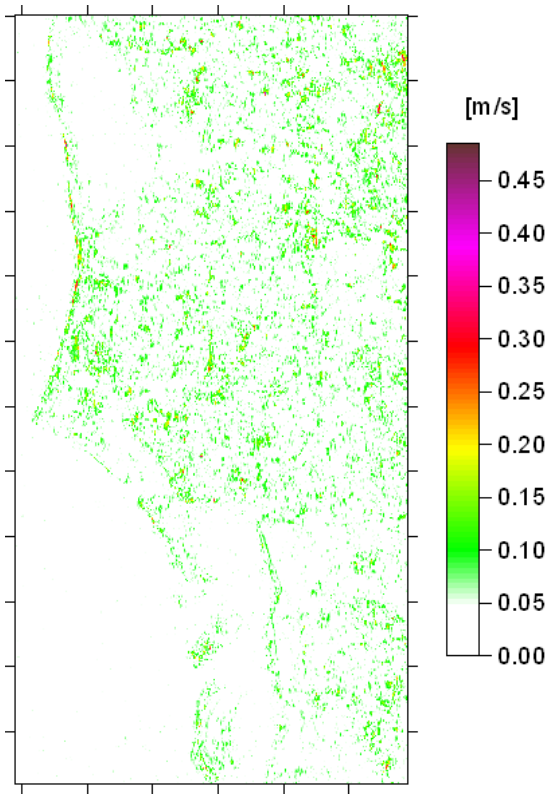

Figure 8: SRTM versus contour map absolute wind speed differences 100 m above ground, 10 m/s mean wind speed.

2.4 Conclusion

The SRTM 3-arcsecond maps, freely available from the US Geological Survey, compare well with the more classical derived maps in this comparison, and are well within the stated goal of less than 16 m error for 90% of the area. For the rather steep Rioja site, 96% gets below the 16 m error, and for the rather flat Western Jutland it is virtually 100%. It is interesting, however, that the mean difference is smaller in the Rioja region than in Jutland. The maps do need a careful survey, however, before being applied, as some of them contain voids, i.e. areas with unknown heights, set to -32768, and they may also contain spikes and wells, i.e. erroneously high and low single pixel values. Such areas and pixels need special care.

Given that the resolution of 3-arcsecond is adequate, the application of the LINCOM code 100 m above terrain indicates that the prediction of wind resources shall change very little over most of the treated areas when using the SRTM data instead of the contour map.

3 Generation of contour maps

The natural format of satellite Earth observation data is raster maps, which actually is appropriate for many flow models. The Risø WASP programme does however require map data in a contour format, and, since this program is widely used in the context of wind resource assessment, map contouring methods are of practical interest. Two slightly different algorithms are considered here - one for interpolating height contours and one for detecting segments with common roughness classification. As an introduction, we briefly describe the WASP program and its use of terrain data.

3.1 WASP modelling

The WASP model analyses meteorological data and estimates the wind energy potential at potential wind energy sites. Typical inputs are wind measurements by instruments on masts operated by airports, national meteorological institutes, or wind energy developers. A regionally representative wind climate is estimated by corrections for local effects of topography, surface roughness, obstacles, and atmospheric stability. Similar inverse corrections, representative for the potential wind energy site, are made in the prediction phase. Terrain-induced wind speed up and obstacle shelter are both modelled by linear flow models and the effects on the wind distribution are relatively simple. The overall effect of terrain roughness is modelled by the geostrophic drag law, which links velocities in the surface layer to the free wind above. The parameters of the geostrophic drag law are the Coriolis parameter and the surface roughness, which both are fixed for a given site, plus the additional effect of atmospheric stability, which depends on wind speed and surface heat flux. WASP accounts for time-dependent stability by a combination of perturbation calculus and, in coastal areas, also a spatial interpolation between inland and offshore heat-flux conditions. The distinction between stability effects at inland and offshore sites is important, because the time scales of relevant surface-temperature changes are substantially different. The effect of upstream surface-roughness changes is modelled by internal boundary layers.

When the wind conditions are determined, the energy production is predicted by a turbine-specific power curve, which describes the generated power for a representative air density as a function of the 10-min averaged wind speed at turbine hub height. The annual energy production of a single turbine is calculated as the convolution of the statistical wind distribution and the power curve. The production of a wind farm also involves a wake model, which accounts for the sheltering effect of upstream wind turbines. This wake model is based on a momentum balance for each wake controlled by a turbine-specific thrust coefficient, which, like the power curve, is a function of wind speed. The wind statistics and energy calculations are repeated for a number of wind directions, in order to account for directional dependence of wind speed distribution and above-mentioned corrections.

Earth observation provides maps of topography and surface roughness, and this is a promising prospect for wind energy planning, since map editing is a tedious and time consuming task. When preparing maps for WASP it is relevant to know that the wind field is more sensitive to local features than to details at greater distance. This is why the flow model of WASP has enhanced resolution near the site of interest. In technical terms, the focus on local details is obtained by a terrain model based on a series of Bessel functions centred at the site of interest. Furthermore, the number of roughness changes

for each wind-direction sector, and thereby the number of internal boundary layers handled by the model, is limited by a maximum value. It is not wrong to feed excessively detailed roughness maps into WASP, since the program has an internal aggregation routine, but the redundant information is unnecessary and computations may slow down. The format of a WASP map file is a number of terrain contours plus a set of 'roughness contours' oriented with distinct roughness categories on their left- and right-hand side, see Figure 9.

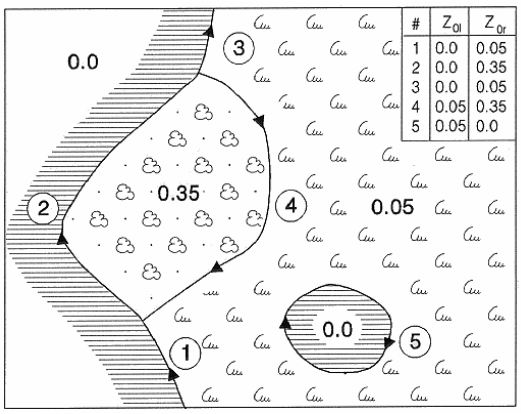

Figure 9. Illustration of 'roughness contours' from the WASP help file.

3.2 Finding contour lines

New software for generating contours from raster maps has been developed and the plan is to include this in the next version of the WASP Map Editor, which is distributed with the main program. With information from digital elevation models, basic contour elements crossing individual cells are constructed as straight lines between the cell boundaries. The contours are organised as expandable coordinate lists, which are managed by a routine for the merging of neighbouring map areas. This routine matches and joins contours at the interface of adjoining areas, and it also recognises closed contours, which need no further manipulation. The program applies the merging routine on larger and larger areas for a suitable range of contour levels until the entire map area is covered. A similar algorithm is implemented for roughness contours, with the difference that these contours follow grid cell boundaries rather than crossing them, and lists of contours are organised for all combinations of roughness classes. Basic roughness contour elements are created whenever the roughness classes of neighbour grid cells differ.

Contour lines need simplification in order to reduce the output file and to minimize the processing time of WASP. The simplification is done by the same method as in the WASP Map Editor, i.e. points are omitted if they are within an acceptable distance from a simplified contour. Points on a line are removed without loss of information and the decimation of curved contours will only introduce a small error.

It is often practical to simplify the raster input before contouring. The first recommendation is to reduce the number of roughness classes to say five classes, since many crops have quite similar roughness lengths, and the usual purpose is to assess the long-term wind climate rather than conditions at the observation time. If the resolution is very fine, it is further recommended to apply a majority filter on the raster map, by which each cell is assigned with the most frequent roughness class in its neighbourhood, e.g. defined as the closest 3 × 3 or 5 × 5 cells. The majority filter tends to remove

isolated segments with minimal modification of larger ones. The majority filter may also remove one-dimensional objects like roads and shelter belts, so the method should be used with consideration.

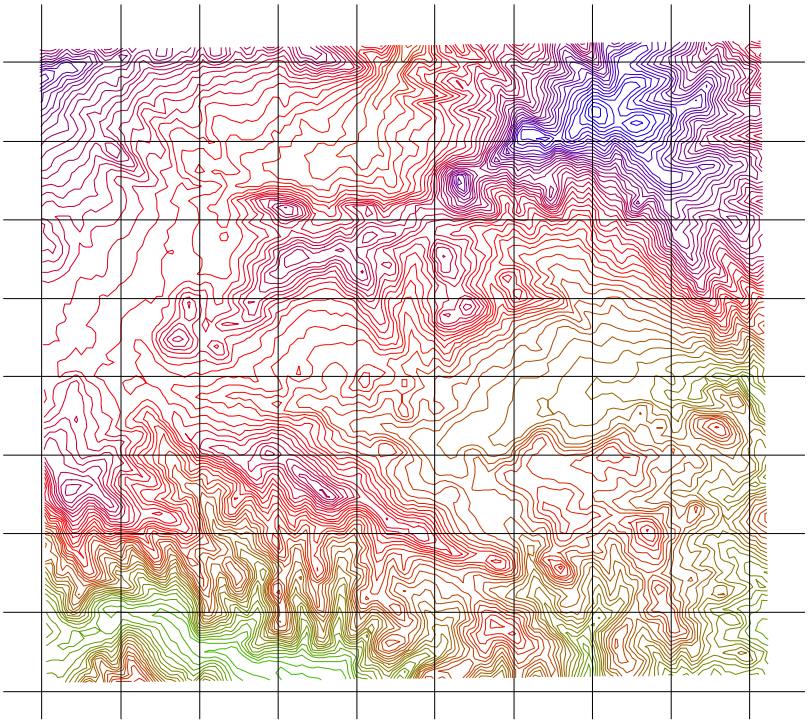

Figure 10. Height contours produced by interpolation of SRTM-3 raster data. The map area is approximately 8 × 9 km and contours are shown for each 10m elevation.

3.3 Examples

Figure 10 shows a new topographic map of the Rioja site also analysed in chapter 2. The contours of the new map are produced with 10 m vertical resolution by interpolation of SRTM-3 raster data, and they are slightly different from those in Figure 1. The number of available pixels is only 132 × 95 pixels and close inspection of the contour map reveals more kinks between contour elements than in the previous hand-made map. The recommendation is to supplement automatic contouring of SRTM-3 data with a detailed map for the area close to the wind farm using the traditional methods of the WASP Map Editor. In many applications this procedure will still be advantageous, since download and automatic contouring is much easier than manual digitization of paper maps.

Figure 11 and Table 1 enable a comparison of various roughness maps of the Foulum area in Denmark. The size of the area is approximately 15 × 15 km and the table lists the resolution of raster input, the number of generated objects, and the size of the output file. The data sources of the first four maps are the CORINE (EEA, 1992) and AIS (NERI, 2001) land-cover databases plus a LANDSAT image. The land-cover information was combined with lists of the aerodynamic surface roughness developed for a previous research project on flux aggregation from local scale to the scale of weather prediction models (Hasager et al., 2003). The roughness evaluation was made after site inspection, which also is the recommended method for future applications. The raster maps were then contoured by the algorithm described above. The last of the five maps was generated in a different way within a project called *Wind Resource Map for Denmark*

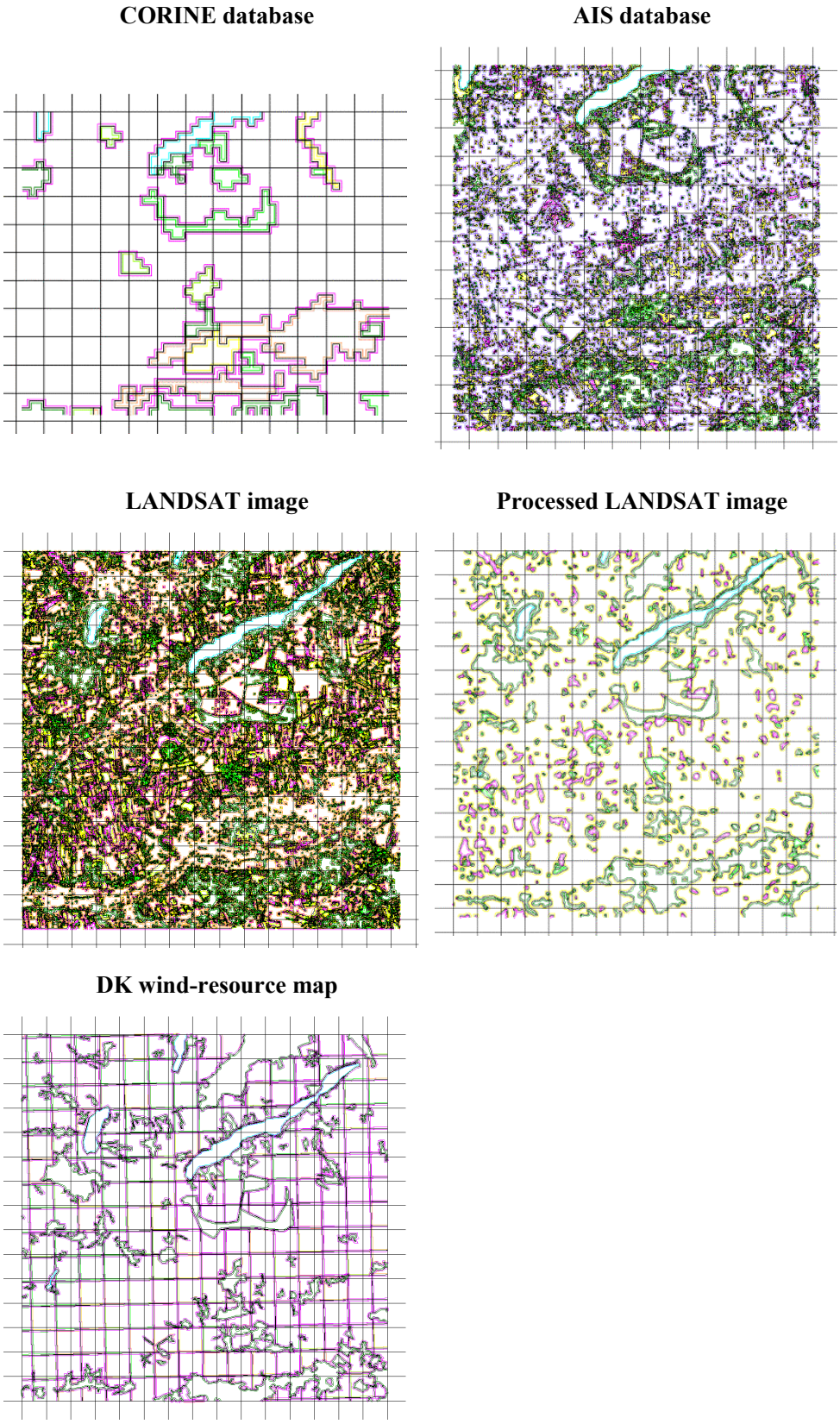

Figure 11. Various roughness maps of the Foulum area (DK).

(Mortensen et al. 1999), and it is included as an illustration of the level of detail preferred by skilled WASP users. By comparison, the CORINE map seems too coarse whilst the AIS and LANDSAT maps seem unnecessary detailed for wind resource assessment with WASP. The simplified version of the LANDSAT image - obtained by class grouping, a majority filter, and contour simplification - is more appropriate.

Table 1: Features of the maps shown in Figure 11.

Source	DK wind-resource map	CORINE database	AIS database	LANDSAT image raw	LANDSAT image processed
Input raster	N/A	250 m	25 m	20 m	20 m
Nodes	16366	478	101980	243402	23018
Lines	485	51	22189	55492	3455
Classes	233	7	8	7	5
File size	416 kB	10.6 kB	2.7 MB	6.5 MB	459 kB

4 Offshore wind statistics by radar images

The surface wind speed and direction over oceans are measured by radar-satellites. The principle of operation is that the backscatter of the C-band of the radar signal (5.3 cm wave length) is a function of small-scale surface waves in the capillary and short gravity wave spectrum, which in turn are functions of wind speed. The two main Earth observation products are SAR (Synthetic Aperture Radar) and scatterometer images. Scatterometer data have less resolution than SAR data but each scatterometer image covers a larger area so data availability for a specific site is generally better. The empirical CMOD model predicts wind speed with an accuracy of ±2 m/s and wind direction within ±20º provided that the wind speed is in the range 2-24 m/s (Stoffelen and Anderson, 1997). An a-priori estimate of the wind direction is needed and this is provided by 2-D FFT (Gerling 86) or wavelet analysis (Du et al. 2002). These methods do however have 180º ambiguity, which must be resolved by the user.

Software was developed and validated within the EU-funded project *WEMSAR - Wind Energy Mapping using SAR* (Hasager et al., 2004) during the years 2000-2003. The Nansen Environmental and Remote Sensing Center (NERSC) developed software for the calculation of wind maps from precision format ERS-1 and ERS-2 SAR PRI images and Risø developed the RWT program (Risø WEMSAR Tool) to derive wind statistics from the NERSC images.

The SAR images has speckle noise, i.e. random variations of individual pixels. As a compromise between noise reduction and high image resolution the WEMSAR project decided to operate on images with 400 m resolution.

4.1 Spatial averaging by footprint theory

The satellite observations reflect conditions at the water surface. The wind at the turbine hub height is different, not only because of the vertical wind profile but also because of the internal boundary layers, which sometimes are present e.g. when the surface wind accelerates away from the coast. If we assume that momentum flux is analogue to the flux of a passive scalar like humidity, micrometeorology offers a theory for the relationship between winds at turbine hub height and close to the surface. With the moderate changes of the flow field, this assumed analogy is almost correct. The theory is known as the footprint model, because the sensitivity of a signal at an elevated point to upstream surface conditions is determined by the same equations as the case of surface exposure during continuous emission at the elevated point with reverse wind direction. Dispersion in the boundary layer depends on wind profile and eddy diffusivity and especially the latter of these conditions are quite sensitive to atmospheric stability. Horst and Weill (1994) developed a reasonably accurate footprint model based on surface-layer scaling, and this model demonstrates that the footprint area is smaller and closer to the observation point in convective conditions whereas it is much more extended during stable conditions. However, as long as boundary-layer stability information generally is unavailable, it seems safer to use the classical model of Gash (1986) describing the footprint in the neutral boundary layer.

The SAR wind raster image is usually not aligned with the wind direction, and for ease of computation the footprint average is calculated as the integral response of a set of observation points distributed with density in accordance with the footprint function. The image information is invalid in shallow waters and the user of the RWT program is

asked to specify a screening polygon for each image. Points beyond this boundary are excluded from the footprint integral, which finally is corrected by the footprint integral of a step function with unit value inside the screening polygon and zero outside.

4.2 Wind speed statistics

Unfortunately, SAR image observations at a specific site are relatively infrequent and the satellites have not yet been in operation for a period representative for the long-term climate. The uncertainty of estimated wind-speed distributions based on relatively few observations were studied by bootstrap statistics of random samples from a long time series of measurements on an offshore mast and also by probability theory (Barthelmie and Pryor 2003; Pryor et al 2004). The problem was formulated as the accuracy of the fitted Weibull distribution, and the conclusion was that the number of samples needed to fit the parameters with ±10% accuracy and 90% confidence was approximately 75 for the Weibull scale parameter and 175 for the Weibull shape parameter. At present, the preparation of this amount of images requires considerable manual work, and, unfortunately, the obtained accuracy is insufficient for wind resource assessment. Another result of the tests were that various Weibull fitting methods provide different accuracy. The most accurate methods were match of observed and theoretical moments and the maximum-likelihood method. The ML method has the further advantages that it may estimate the true distribution of censored data without bias (e.g. Cohen, 1965; Appendix E), and this is relevant because SAR data are limited to a range of wind speeds.

The measure-correlate-predict method might be a way to mitigate the problem of poor statistics due to sparse observations. The general idea is first to establish a correlation between local data at the site of interest and reference data from a nearby station with a long data record, and then to use the correlation model to predict on-site wind statistics representative for a long period. This has not yet been attempted, but the method is well known in the context of wind resource assessment where developers often measure local winds for some years before the wind farm construction. The expectation is that the correlation between winds at an offshore site and a coastal reference station depends on wind direction and probably also on season and the time of day because of the time-dependence of the stability effect.

Another approach is to look for spatial trends in maps of wind statistics. The expectation is that the wind resource improves with the distance from the source, as in the WASP program, and the exact nature of this transition is of interest. Repeated use of the basic footprint-averaging method at a multitude of positions is inefficient, so a complementary method based on Fourier transformation was developed. The response integral is calculated as the convolution of the wind field and the footprint mask mirrored around the crosswind direction. Polygon screening was implemented by setting the wind speed outside the boundary to zero before convolution with the footprint function. The only limitation of this method is that it can not model a possible spatial variation the footprint filter.

4.3 Directional variation

The shortage of data is also a problem for determination of directional distributions. The usual procedure in a WASP analysis is to divide the data into twelve bins for 30 degree wind direction sectors and determine the Weibull wind-speed distribution for each of these. The number of satellite observation in a single bin could be very small so for the

RWT program it was decided to fit a distribution to all data and use the shape parameter for every sector. The scale parameters were then estimated by the average wind speed in each sector. The frequency of occurrence in each sector is uncertain when observations are sparse and there is a risk of observing sectors without any observation and no estimate of the mean wind. An alternative to simple bin counting is to sort all observations after direction, estimate the probability density between the observations by the angled separating between them, and finally resample the densities in the standard sectors.

5 Examples using SAR images

At the Horns Rev site in the North Sea, 80 2MW wind turbines started operation in December 2002 http://www.hornsrev.dk. Prior a meteorological time-series was collected by Elsam Engineering (Sommer, 2003). The meteorological time-series is unique. It is of high quality and designed for offshore wind resource mapping. Based on this meteorological time-series, it was chosen to investigate the validity of using SAR images for wind mapping in the WEMSAR project http://www.risoe.dk/vea-atu/remote/wemsar.htm. A series of 61 ERS SAR satellite images were compared to observations at the mast (Hasager et al. 2004b). As described in section 4.1, it is important to average the wind data in the satellite wind map with a footprint method, in order to achieve wind observations that are comparable to a certain point in space. Footprint averaging was used in the analysis. The comparison results show a negative bias ~0.3 ms^{-1} in the SAR wind maps and a standard error ~ 1.3 ms^{-1}.

A mean wind speed map based on the 61 satellite wind maps all retrieved prior to construction of the wind farm, is shown in Figure 12a and the number of images in Figure 12b. It is interesting to notice that the mean wind speed decreases from far offshore to near the coastline. The decrease is from 7.6ms^{-1} to 4.6 ms^{-1}. The decrease is comparable to results from a simple geostrophic drag law calculation combined with a logarithmic wind profile near the surface giving 8.1 ms^{-1} far offshore and 4.5 ms^{-1} far inland (at 10 m height), assuming a surface roughness of 2 $*10^{-4}$ m and 0.2 m over sea and land, respectively, and a geostrophic wind of 12 ms^{-1} (pers. com. Niels Otto Jensen) (Hasager et al. 2004e).

An additional series of 24 ERS SAR satellite images were received within the SAR-WAKE project http://www.risoe.dk/vea-atu/remote/sar-wake.htm for investigation of the wake effect from the large offshore wind farm (Christiansen, 2004; Christiansen and Hasager, 2004). Combining the two datasets and focusing on areas without any influence of the wind farm, new results are obtained. This work is part of the SAT-WIND project http://www.risoe.dk/vea-atu/remote/sat-wind.htm. Currently 85 ERS-2 SAR wind maps are used in the study.

The new mean wind speed map based on 85 ERS-2 SAR wind maps is shown in Figure 13a and the number of samples in Figure 13b. This time the figures are taken directly from the RWT software described in chapter 4 and in Hasager et al. (2004d). Several items can be noticed in Figure 13a. First of all the ‘squares’ clearly show the position of the satellite images. These images are always recorded at a small angle from true North as the satellite is inclined in its polar orbit. Each image is 100 km by 100 km. In the image positioned northwest, it is possible to see some blue-purple striping. It shows a single satellite image and reveals the wind direction streaks aligned with the wind coming from the northwest at the time of the satellite recording.

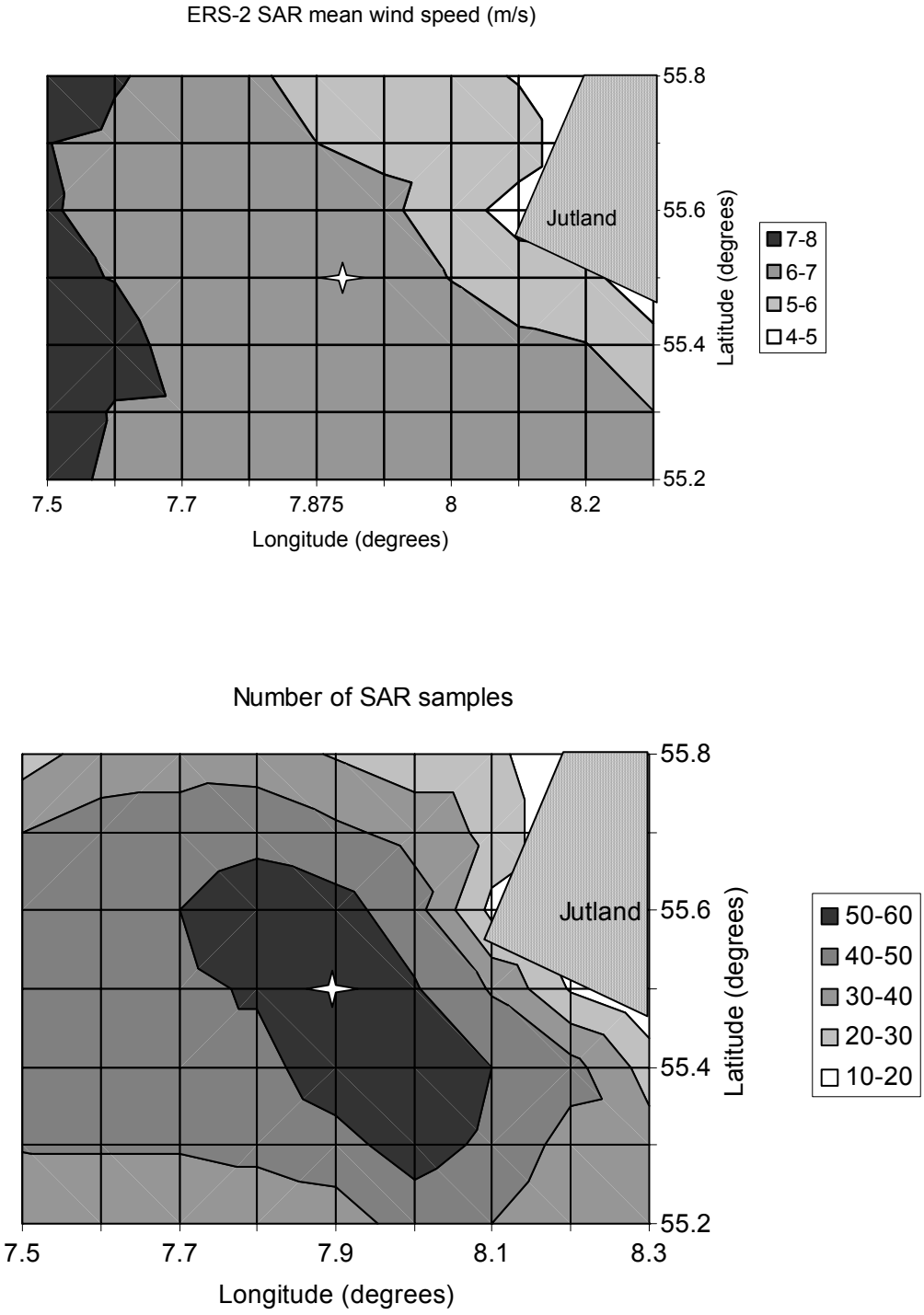

Figure 12 a) Mean wind speed map at 10 m based on 61 ERS-2 SAR satellite wind maps for the Horns Rev area, and b) Number of satellite images (samples). The meteorological mast is located at the white star.

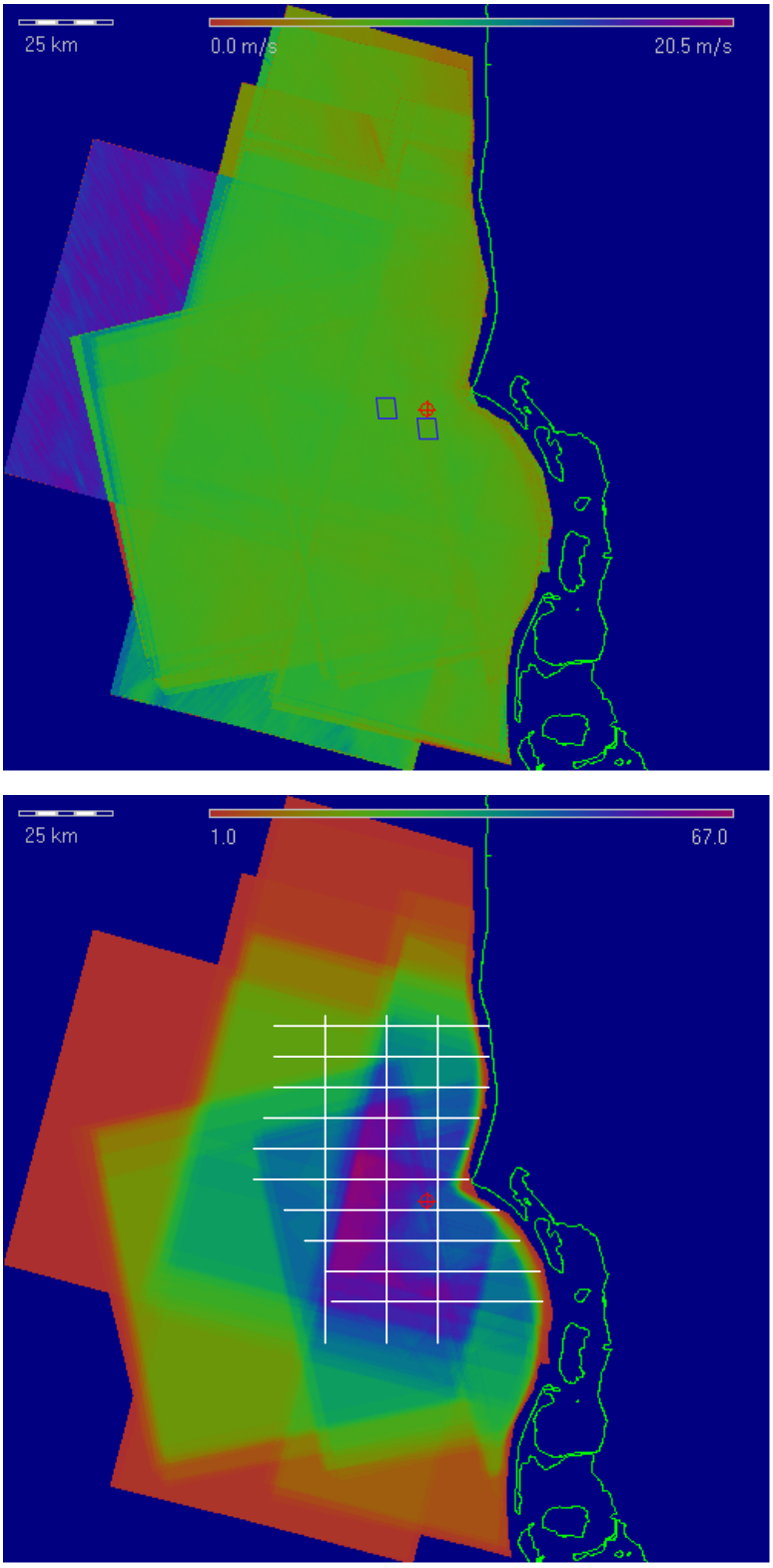

Figure 13 a) Mean wind speed map at 10 m based on 85 ERS-2 SAR satellite wind maps for the Horns Rev area, and b) Number of satellite images (samples). The meteorological mast is located at the red crosshair. The outline of the present (eastern) and prospected (western) wind farm is indicated in a), and the ten horizontal transects west to east, and three north to south are indicated in b).

Each satellite images is recorded within 15 seconds, hence they are virtual snapshots of the meteorological conditions. The mean wind data from the ten horizontal transects are selected (see Figures 13b) and averaged for a study on spatial variation in wind speed statistics (mean wind speed, Weibull A and k) from offshore to the coastline. Also three horizontal transects from north to south are extracted and averaged. The results are presented in Figures 14a and b, respectively.

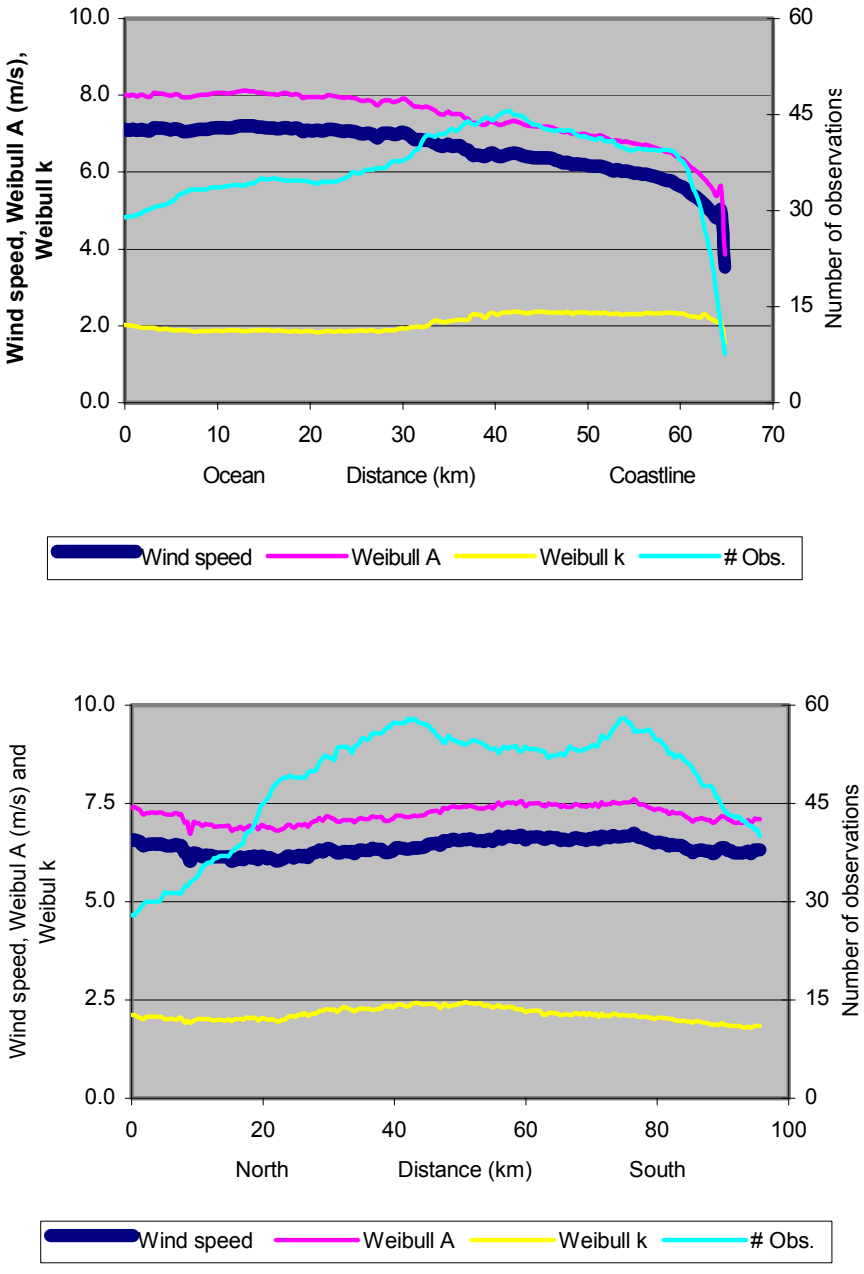

Figure 14 Results from horizontal transects a) from west to east, and b) north to south based on 85 ERS-2 SAR wind speed maps. The mean wind speed, Weibull A, Weibull k and average number of observations is included. Number of observations is shown on the secondary y-axis.

From figure 14a a general increase in mean wind speed is found from the coastline and offshore. It seems to be increasing also at a distance of 60 km offshore, however the largest increase appears near the coastline as expected. Weibull A is also increasing offshore whereas Weibull k is decreasing from 2.3 to 1.9. The north to south transect in figure 14b shows a slight variation in wind speed, Weibull A and k over a distance of 100 km. The number of observations also varies and some of the variation found could be due to the number of samples.

5.1 Quantification of spatial gradients based on subsets

In the next part of the study, two subsets of ERS SAR wind maps are used for a comparison of wind statistics from the center of the present wind farm, the center of the prospected wind farm, the four corners of each wind farm site and the meteorological mast (see Figure 13a for the locations). The prospected wind farm coordinates are found from a map at http://www.ens.dk (Danish Energy Authority). The two subsets consist of 47 and 30 wind maps recorded prior to construction of the wind farm. Figure 14a and shows the polygons delineating the 47 and 30 wind maps, respectively. The results on mean speed are shown in Table 2.

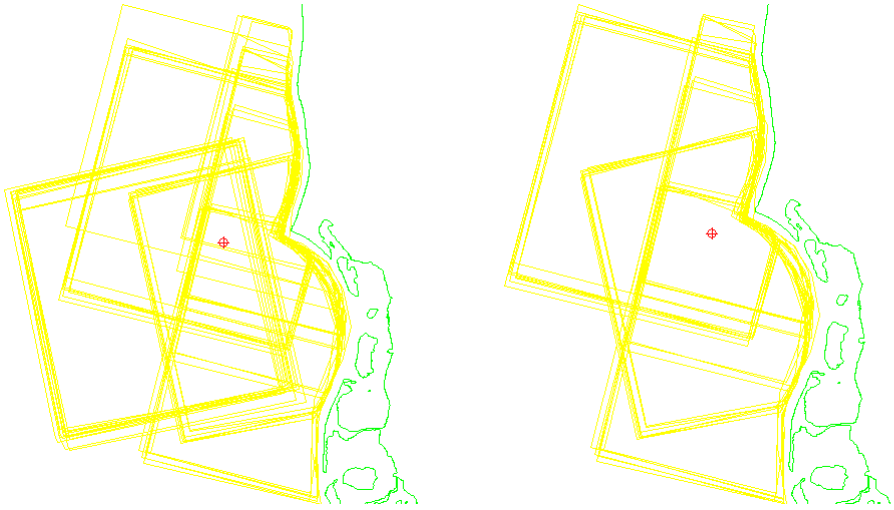

Figure 15 Maps of polygons from ERS-2 SAR wind maps recorded prior to construction of the Horns Rev wind farm a) 47 wind maps with the crosshair at the centre of the prospected wind farm; b) 30 wind maps with the crosshair at the centre the present wind farm.

Table 2. The corner coordinates of the prospected wind farm are called N1 to N4, for the present wind farm P1 to P4. The center coordinates CN and CP for the prospected and present wind farm, respectively. M is for mast. The values are mean wind speed in ms^{-1} from 47 (in bracket from 30) ERS-2 SAR wind maps.

			M 6.50 (6.68)		
N1 6.71 (6.73)		N2 6.65(6.76)	P1 6.44 (6.60)		P2 6.38 (6.59)
	CN 6.67 (6.79)			CP 6.36 (6.55)	
N4 6.76 (6.90)		N3 6.57 (6.72)	P4 6.47 (6.66)		P3 6.37 (6.56)

Spatial variation in mean wind speed is found over the investigated area (Table 2). Lower winds are found southeast and higher winds southwest. The mean wind speed at the centre of the prospected wind farm is 4.9 % higher seen from 47 wind maps (or 3.7%

seen from 30 wind maps). The distance between the two points is ~ 11 km. As the uncertainty on the mean wind speed is ~0.4 ms^{-1} using 47 maps and ~0.6 ms^{-1} using 30 wind maps, the 4.9% is thought to be slightly closer to the truth. The uncertainty mentioned above is only related to the low number of samples and for the assumptions that the wind maps are error free and randomly sampled. Neither of the two assumptions hold true. Firstly it is shown (Hasager et al. 2004b) that the uncertainty (standard error) in the wind speed maps is 1.3 ms^{-1} comparing 56 wind maps to *in-situ* data and the bias is –0.3ms^{-1}. Secondly the images are not recorded randomly but either around 10 UTC or 21 UTC.

Spatial mean wind speed variations are investigated in more detail in the following, attempting to estimate the rate of change in mean wind speed from the coastline and offshore as seen in the 47 ERS SAR wind speed maps. Figure 16a shows the number of images (up to 47 in the central part), and Figure 16b shows the uncertainty estimates on wind speed, ~0.4 ms^{-1} in the central part and increasing in areas with lower number of images.

The results from the horizontal transect line indicated in Figure 16b is displayed in Figure 17. It is interesting to notice that there is a steady increase in mean wind speed from ~ 20 to 40 km offshore and the number of images is constant in this zone. The mean wind speed is also increasing from ~70 to 100 km offshore but for this area the uncertainty is much higher and the number of images very variable. Therefore it is less certain that an increase in mean wind speed actually occurs with such an accelerated rate.

The coastal zone from 3 to 35 km is of general interest for offshore wind farming. Therefore a detailed analysis of the increase in mean wind speed for this zone is performed. Results from two additional horizontal transect lines very close to the horizontal transect in Figure 16b, are shown in Figure 18a. Some variation between the three transects is found especially close to the coastline. The average of the three transects is calculated and shown in Figure 18b including two fitted curves. One is an

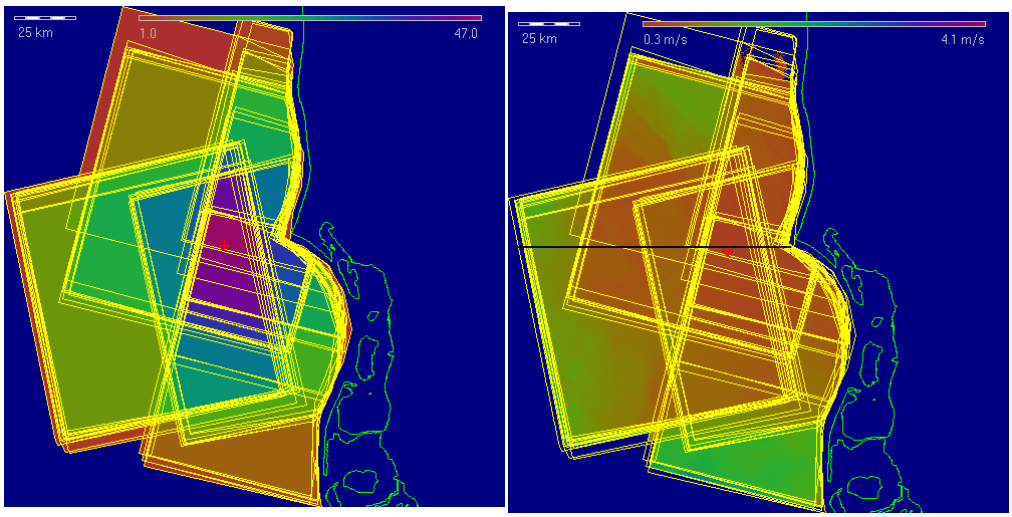

Figure 16. The polygons and a) number of wind maps from ERS SAR (up to 47) and b) uncertainty estimate on mean wind speed for the Horns Rev site. Only images prior to construction of the wind farm are included. The red crosshair is at the centre of the prospected wind farm, and location of the horizontal transect line is shown in b).

exponential fit, the other a moving average. Based on these results, the average increase in wind speed in absolute values and in percentage is found for the 5 to 10 km, the 10 to 20 km and the 20 to 30 km zones. The results are listed in Table 3. It is seen that the increase is larger near the coast.

In general it is best to use as many wind maps as possible for the analysis. However for the results plotted in Figure 17 it is clear that 'jumps' are found, e.g. for mean wind speed, Weibull A and k around 65 km offshore. This 'jump' in the curve is related to the variable number of satellite wind maps used. Another way of showing the problem of the number of wind maps is given in Figure 19a and b that shows the mean wind speed map based on 47 wind maps. Only within the area delineated are all 47 wind maps available. Figure 19a gives a very clear impression of the problem.

Therefore a subset of only 30 wind maps out of the 47 is then used to calculate wind resource statistics. It provides a large area covered with a constant number of samples. The mean wind speed map based on 30 wind maps is shown in Figure 19c and d. Figure 19d. Figure 19d contains indication of the position of the present and prospected wind farm and a horizontal transect line.

Table 3. Increase in mean wind speed as a function of distance from the coastline measured by 47 ERS SAR wind speed maps.

Distance	Absolute (ms^{-1})	Percentage
5 to 10 km	0.22	3.7
10 to 20 km	0.21	3.3
20 to 30 km	0.18	2.7

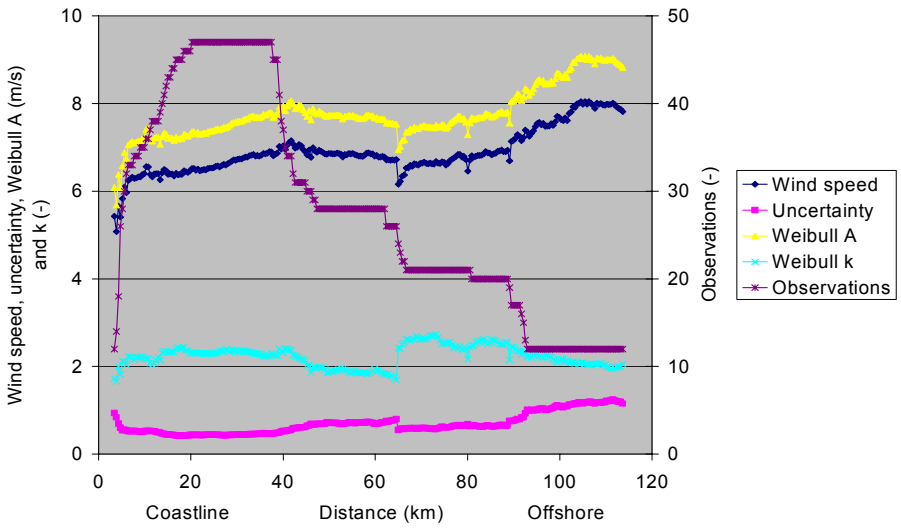

Figure 17 Wind speed statistics from the coastline and offshore based on 47 ERS SAR wind maps. Number of observations is shown on the secondary y-axis.

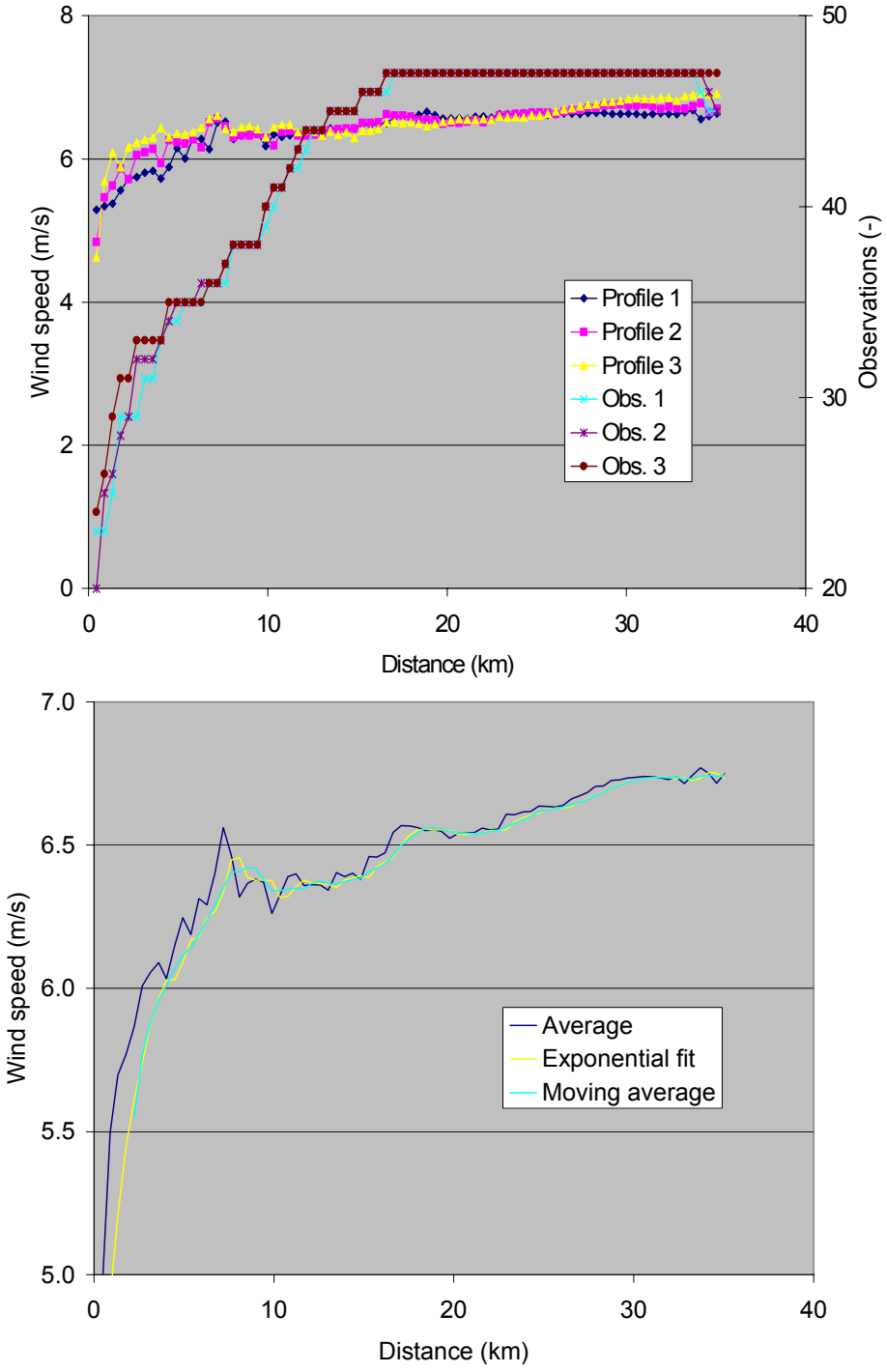

Figure 18 Mean wind speed from a) three parallel transects near Horns Rev from the coastline and offshore. The number of observations is shown on the secondary y-axis. b) the mean wind and two fitted curves, one with exponential fit with damping factor 0.5, the other a moving average with interval 5. The results are based on 47 ERS SAR wind speed maps.

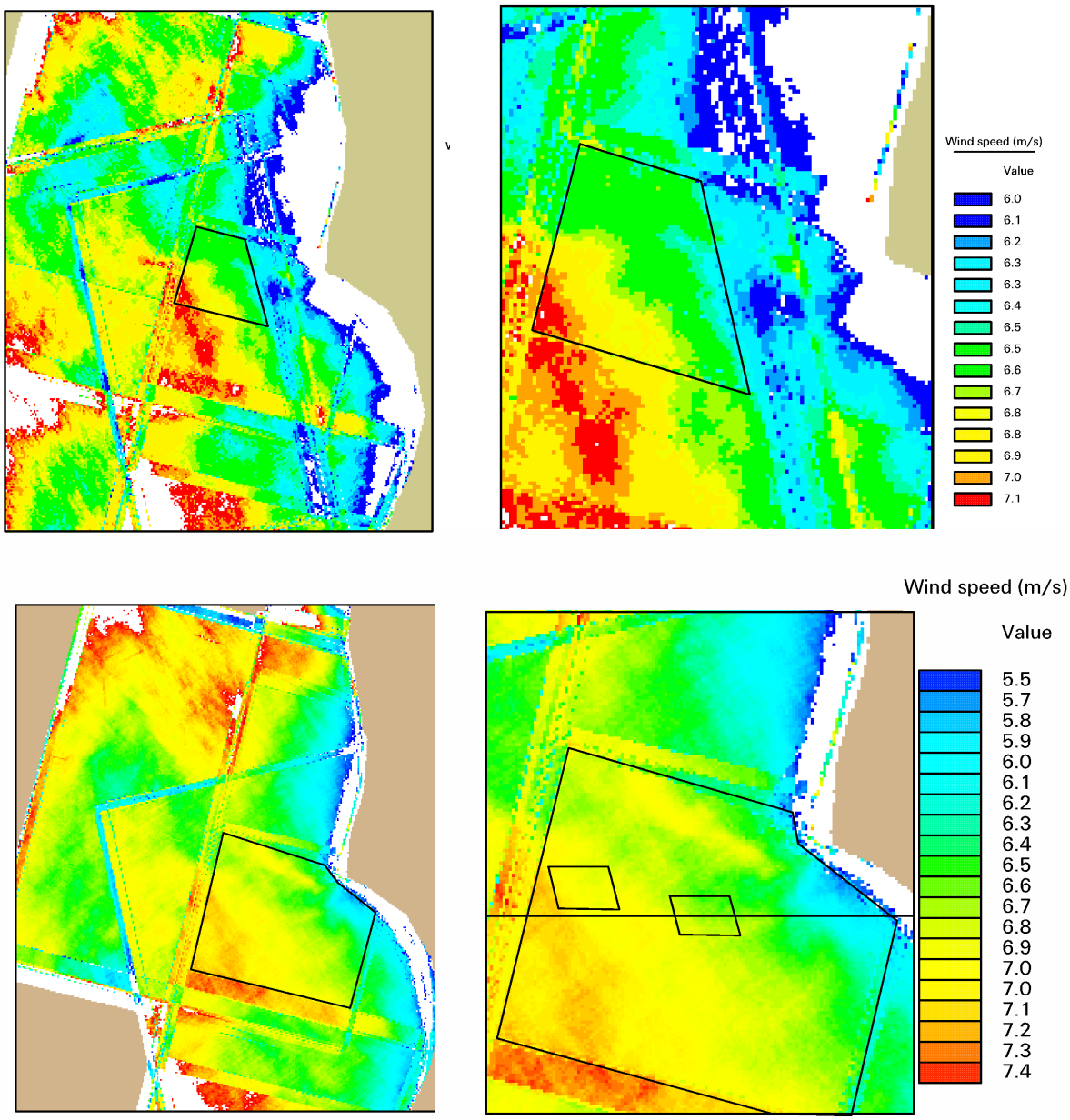

Figure 19 Mean wind speed maps based 47 ERS SAR images upper panel: a overview and b zoom. Lower panel: based on 30 wind maps. In d) indication of location of the present and prospected wind farm and the horizontal transect line. Please note the color scales are different for the upper and lower panels.

The mean wind speed maps (Figure 19) show the average wind to increase offshore as a function of distance to the coastline. The curved nature of the coast of West-Jutland is found rather clearly in the wind speed variation offshore at least up to a distance of 60 km. In order to quantify wind statistics at larger distances offshore an additional analysis is needed. (It could be based on another subset of the 85 available wind maps but it is not done in the current work). Focus is here on the wind farm area.

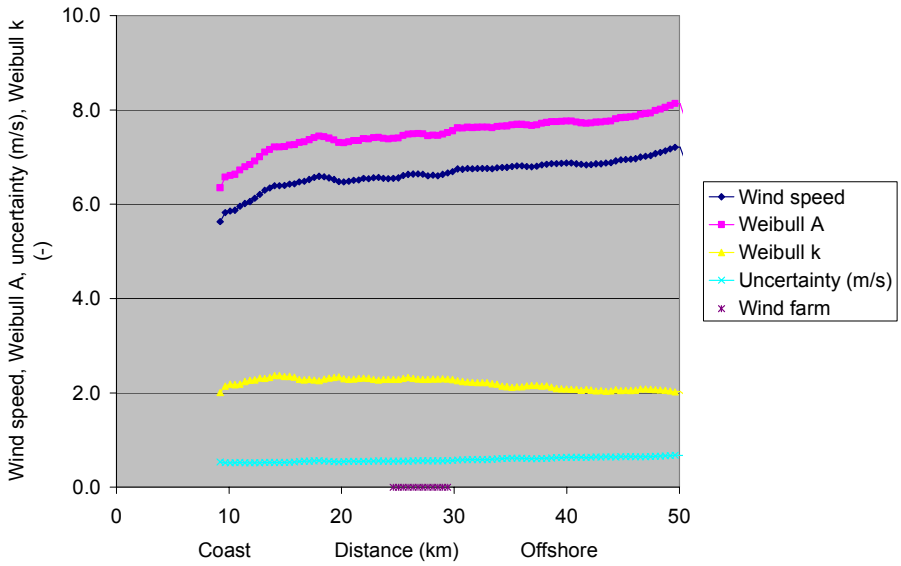

Figure 20 Wind statistics along a horizontal transect line from the coast and through the Horns Rev wind farm based on 30 wind maps from ERS SAR collected prior to construction of the wind farm.

Result on wind statistics from the transect line (see Figure 18d) is given in Figure 18. It shows an increase in mean wind speed and Weibull A from the near-coastal zone to 50 km offshore. In the zone from 10 to 18 km offshore, the increase is ~ 14 % whereas the increase in the zone from 20 to 50 km offshore is ~ 8 % for mean wind speed. Weibull k decreases from ~ 2.3 to ~ 2.0. It is a decreases ~ 13 % from 14 to 50 km offshore.

Finally wind resource statistics based on 47 wind maps are listed in Table 4 for the centre of the present and prospected wind farm site. Two Weibull fitting methods are applied. The maximum-likelihood (ML) has the advantage that the number of censored data (either with too low or too high winds) can be included prior to fitting. The first and third order moment fitting gives a precise mean wind speed. The wind maps show that the energy density is ~ 11% higher at the centre of the prospected site than at the centre of the present site (using ML fitting). The increase in mean wind is (as mentioned before) ~ 4.9% higher (using 1&3 order moment fitting). In this case no observations were censored out, however in case that is necessary, ML fitting is to be recommended.

Table 4. Wind resource statistics based on 47 ERS SAR wind speed maps from the centre of the present and prospected wind farm at Horns Rev, Denmark. The uncertainty estimates are given in brackets. The wind data have been fitted with maximum-likelihood (ML) and 1&3 order moment fitting.

	Unit	Present wind farm		Prospected wind farm	
		ML	1&3 moment	ML	1&3 moment
Mean wind speed	m/s	6.0 (0.4)	6.4 (0.4)	6.4 (0.4)	6.7 (0.4)
Weibull scale A	m/s	6.8 (0.5)	7.2 (0.5)	7.3 (0.5	7.5 (0.5)
Weibull shape k	-	2.1 (0.2)	2.3 (0.3)	2.3 (0.3)	2.3 (0.3)
Energy density	m3/s3	398 (85)	437 (85)	443 (83)	493 (93)

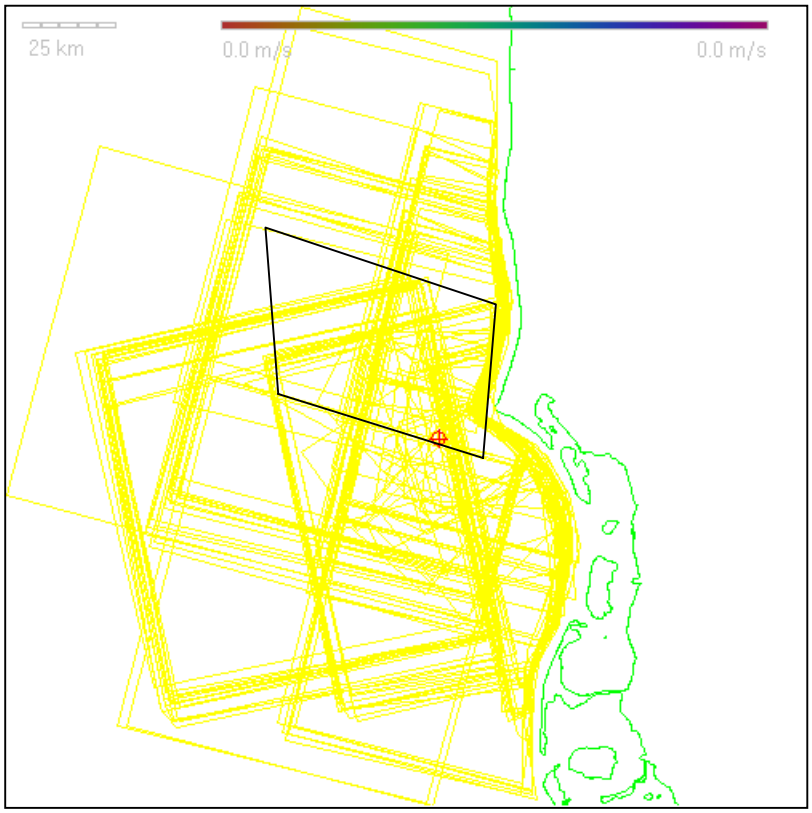

Figure 21. Yellow polygons show the location of 85 ERS SAR wind maps. The brutto-area is indicated with a black polygon and the red crosshair is at the centre of the present wind farm at Horns Rev, Denmark.

The area indicated by The Danish Energy Authority (http://www.ens.dk) as the so-called brutto-area in which a new wind farm may be constructed is shown in Figure 21. There are slightly less than twenty images (morning scenes only) that cover the whole area within the 85 wind maps. It would be easy to order a set of images that cover the whole area and include morning and evening passes in this selection. Further investigation based on the current data set is in progress. Within the study on optimal offshore wind energy developments in Belgium the area of interest can also be map from ERS SAR. One typical morning scene is shown in van Hulle et al. (2004).

Hence for investigations such as the current at Horns Rev and the Belgium case, ERS SAR (and Envisat ASAR IMG and APP) has an adequate grid resolution and spatial coverage.

5.2 Summary on wind resource statistics based on SAR

Wind resource mapping based on satellite SAR images alone will be very uncertain. This study is based on 85 wind maps. The new results are very promising, in relative terms, as significant spatial variations in the offshore wind resource statistics at the Horns Rev wind farm site are identified.

As an example the mean wind speed is found to be ~ 4.9 % higher and the energy density to be ~ 11 % higher at the centre of the prospected wind farm compared to the centre of the present wind farm at Horns Rev at 10 m above sea level. The distance

between the points is ~ 11 km. In general terms, the mean wind speed increases offshore with the highest increase closer to the coastline but still increasing 50 km offshore.

5.2.1 On limitations

Limitations are the

- number of available images,
- accuracy of each wind map (compared to *in-situ* meteorological data),
- fixed recording times twice during the day.

A large number of images are available from the ESA archive hence this limitation can be overcome in future work. Especially if combining the ERS and Envisat data. Several hundred images are already available for some areas of the globe.

The accuracy on wind speed in each map is currently being improved within the satellite community, however wind mapping most likely cannot be much better than ± 1 ms^{-1} in absolute terms due to inherent properties of the SAR data, long- and short ocean wave patterns and wind retrieval algorithms. Correction for e.g. atmospheric stability effects for offshore flow in coastal regions could (partly) be accounted for using a modelling approach. Work is in progress.

Finally the fact that SAR wind maps only are available at two fixed times during the day could be corrected for if a wind data time-series is available from a nearby site.

5.2.2 On advantages

Advantages are that

- wind maps with high spatial detail are available,
- there is quick access to the information.

Wind resource statistics obtained from satellite SAR images are unique. Wind speed maps with very detailed spatial information can only be obtained through SAR.

The amount of reliable offshore wind data is very sparse due to the high cost on construction and maintenance of offshore meteorological masts. Therefore offshore wind resource model results could in fact be verified to the wind maps from satellite SAR in addition to validation to the point observations from high quality data at offshore masts.

The satellite wind maps are representative for 10 m above sea level. The footprint modelling ensures that the SAR-based wind information resembles time-series meteorological data. Extrapolation to hub-height will have to be done with e.g. WASP including coastal terrain effects (topography and roughness), in order to assess the wind power potential. Software is now developed for practical use.

The satellite SAR images are available to all users within a few days from ESA. The newly developed software within the EO-windfarm project provides wind engineers fast access to information based on satellite SAR wind maps anywhere on the globe. The processing time for a skilled user (e.g. 100 images) would be ~ 2 weeks on a standard pc.

5.3 Recommendations

It is recommended to select SAR images from night and day passes. It is also recommended to check that the area of interest is covered by each satellite image[3]. Wind resource statistics based on SAR wind maps should be checked with nearby coastal (or ideally offshore) wind data or meteorological model data during the processing of the images.

First of all the approximate wind direction needs to be known *a priori* in order to identify the 180º ambiguity in wind direction before the wind speed can be calculated from SAR. Secondly each satellite image should be checked visually for atmospheric and oceanic structures not related to homogeneous (stationary) flow conditions (e.g. fronts, rain cells, sea current, slicks, etc). It is in fact not very difficult but takes some time.

Finally the wind resource statistics from the SAR wind maps should be used with great caution because the absolute uncertainty is very high and not adequate for siting of wind turbines in a stand-alone mode. The information may solely be used to screen offshore areas of interest, e.g. planning where to place an offshore meteorological mast, or to cheaply estimate wind resources between existing offshore wind farms, offshore meteorological masts and nearby sites.

3 Please note that the SAR images can be ***shifted along the track*** (~ North to South) in steps of 5.5 km. For across-track (~ West to East) the scenes cannot be shifted. Instead the next available track should be selected. It is spaced ~ 40 km in either direction. The selection of images is done in EOLI or DESCW at ESA.

6 Comparison of wind speeds from scatterometer, altimeter, global model and in-situ data

This study focuses on a comparison of different satellite derived wind speeds (scatterometer and altimeter) e.g. (Tournadre and Ezraty 1990; Glazman and Greysukh 1993; Guymer and Zecchetto 1993) with data from the NCEP-NCAR reanalysis data set (Kalnay et al. 1996), (Kistler et al. 2001) and with observations from the meteorological mast at Horns Rev (Sommer 2003). This site is located about 20 km west of the western most point of the Danish coast (Figure 22).

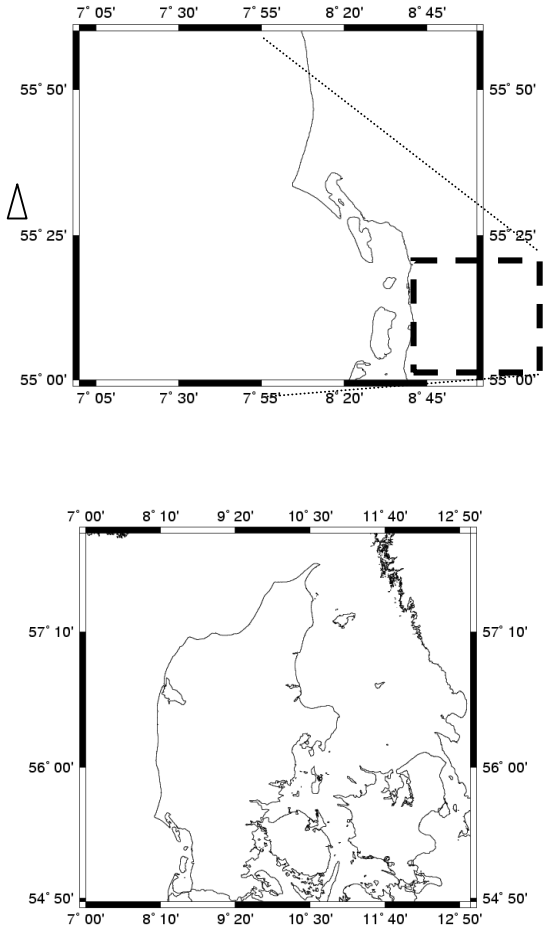

Figure 22. Map showing the location of Horn Rev

There are four major difficulties in making the comparison of the wind speeds derived from remotely sensed observations with the in situ measurements and the reanalysis data:

- Comparison of point measurements from a meteorological mast with areally averaged observations from satellites and a reanalysis model. Due to spatial heterogeneity of flow regimes use of a larger area, particularly if it is further offshore than the meteorological mast, will affect the absolute wind speed

derived from the data. For this reason some of the analysis presented below is focused on variations of normalized wind speeds.

- Variations in the data set density (see Table 5). The reanalysis data are four-times daily, the in situ measurements are hourly averages, while the scatterometer from ERS-1/-2 and NSCAT, and altimeter data from TOPEX/Poseidon and Jason-1 are derived from 343 and 1516 passes, respectively, over a 12 year period with some spatial aggregation. Quickscat scatterometer data were so far only available as monthly averages giving insufficient information for a wind speed or direction distribution, so they are not used in the comparative analyses beyond the seasonal cycle.
- The data sets are characterised by differing levels of precision, minimum detectable limits and accuracy.
- The data periods do not exactly coincide.

6.1 Seasonal variations

As indicated in (Hasager et al. 2004a) there is good correspondence in the month-to-month variation of wind speeds from Quickscat and NCEP-NCAR in comparison with wind speeds measured at the mast at Horns Rev (at 62m) over the period from 2000-2003. Here we repeat this analysis and add wind speeds from altimeter and scatterometer provided by ARGOSS (H. Wensink, personal communication 2004). Figure 23 shows mean monthly wind speeds calculated using the data sources given in Table 5. In making these comparisons it is important to note that NCEP-NCAR assimilate some scatterometer data over the oceans so these data sets (NCEP-NCAR v. scatterometer) are not entirely independent.

Table 5. Details of data sources.

Type	Area	Central location	Height (m)	Data period
Observed	Mast	55.52°N, 7.78°E	62 15	June 1999-December 2003 April 1999 to November 2002
Scatterometer Quickscat	0.5° by 0.5°	55.5°N, 7.5°E	10	August 1999 – December 2003
NCEP-NCAR	1.875°by 1.875°	56.19°N, 7.5°E	10	June 1999-December 2003
Altimeter Topex, Poseidon, Jason, GFO	100 km by 100 km	55.52° N, 7.78° E	10	1991- 2003
Scatterometer ERS	100 km by 100 km	55.52° N, 7.78° E	10	1991-2003

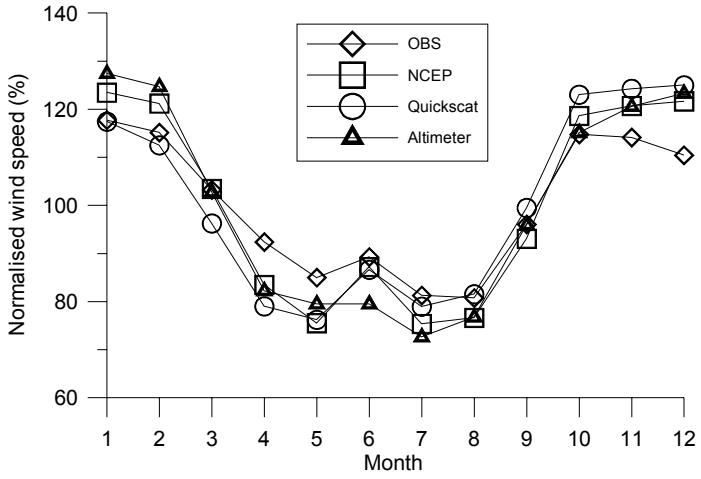

Figure 23. Normalised mean monthly wind speeds from observed, NCEP-NCAR, Quickscat and Altimeter data sets (%). In this image each data set is normalised to the mean wind speed from that data and expressed as a percentage of the mean.

As shown in Figure 23 there is good agreement between the data sets in terms of the seasonal variability. However, the observed data show rather less month-to-month variability than the other data sets. While the absolute range between the maximum and minimum normalized monthly averages from the observed data is 37%, it is 48% for both NCEP-NCAR and Quickscat and 55% for the altimeter data.

6.2 Wind speed and direction distributions from the individual measurement platforms

6.2.1 In situ data

Wind speed and directional distributions from the in situ data at Horns Rev over the period April 1999 to November 2002 are given in Figure 24 (Sommer 2003). As expected the data give a good fit to the Weibull distribution and have a shape factor of 2.3. Dominant wind directions are westerly.

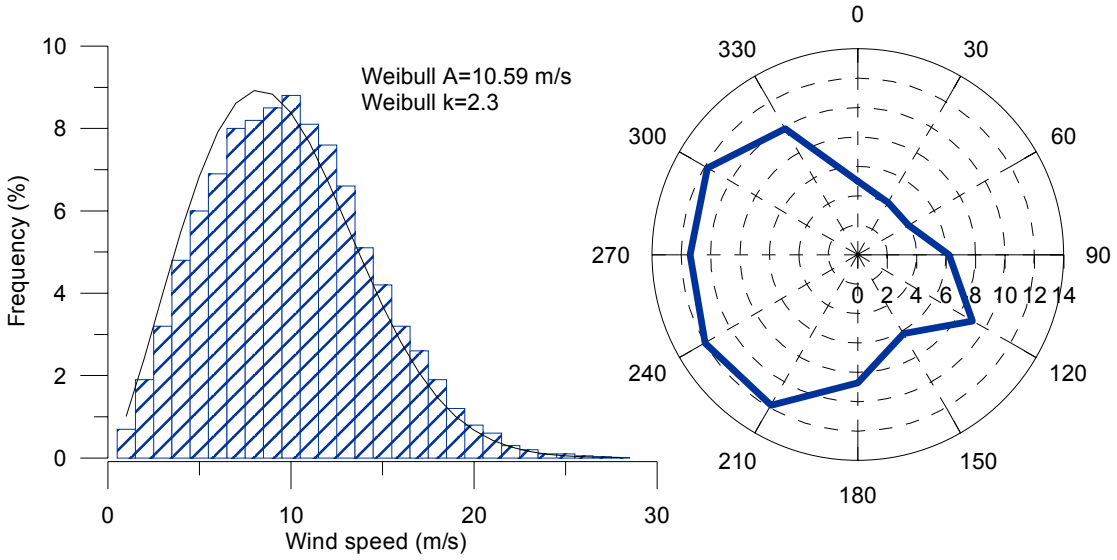

Figure 24. Wind speed distribution and wind direction distribution from observations at 62 m as presented in (Sommer 2003).

6.2.2 NCEP-NCAR

Wind speed data were derived from the u and v components of the NCEP-NCAR data set for two temporal windows: (a) 1996-2003 and (b) June 1999-December 2003. As shown above (Figure 25) the choice between the two data periods has little influence on the Weibull fit or the wind speed distribution. The offset in the absolute value of the Weibull A parameter and mean wind speed (U) shown in Figure 24 and 25 is due to the difference in the wind speed height. In the observations summarized in Figure 24 it is 62 m above mean sea level whereas the NCEP-NCAR data represent a height of 10 m above the surface. The Weibull k parameter which is considerably less variable with height (see (Pryor and Barthelmie 2002)) is entirely consistent between the two data sets. Figure 25 further shows that the quality of fit to the two-parameter Weibull distribution (see description in Pryor et al. 2004) is also excellent in the NCEP-NCAR data.

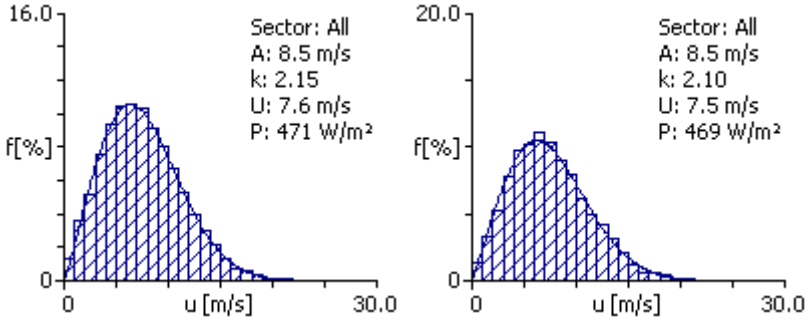

Figure 25. Wind speed distribution from NCEP-NCAR data set for 1996-2003 (left) and for June 1999 to December 2003 (right). Note the change of scale between these two frames.

6.2.3 Scatterometer

Figure 26 shows the wind direction distribution and wind speed frequency distribution for the scatterometer (ERS) from ARGOSS data. As shown, the Weibull A parameter is higher than that derived from the NCEP-NCAR data. This may reflect that the scatterometer scenes were not chosen to give a representative wind climate.

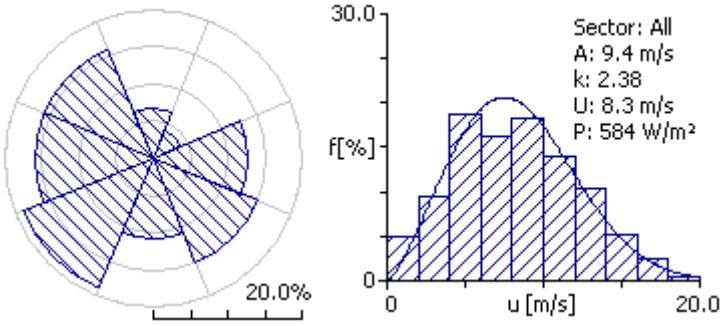

Figure 26. Wind speed and direction distribution from the scatterometer ERS data set.

6.3 Comparison of the data sets

6.3.1 Comparison of the wind direction distributions

Comparing scatterometer with observed data shows good agreement in capturing dominant westerly flow and a south-easterly (120°) component of the wind direction distribution (13% in the altimeter data set 9% in the observed). In total nearly 53% of observations from the scatterometer lie in sectors between 195-345° in the scatterometer data set, and 66% in the observed data sets. In light of differences in the data collection periods, this is deemed to be good agreement.

6.3.2 Comparison of the wind speed and wind speed distributions

Table 6 shows a comparison of 10 m wind speeds derived from the different data sets. Here we utilise data from Horns Rev at 15m since this is the lowest measurement height (from (Sommer 2003)). We use a a factor of 0.96 to determine the approximate 10 m wind speed and Weibull A factor from 15 m levels. It gives a wind speed and Weibull A factor of 7.6 m/s and 8.7 m/s from the observations – however the observing period April 1999 to November 2002 may not be representative although it is in good agreement with data from NCEP-NCAR.

Table 6. Comparison of wind speeds at the Horns Rev using the different methods

Type	Weibull A (m/s)	Weibull k	Mean wind speed (m/s)
Observed (15m)	8.98	2.2	7.89
NCEP-NCAR	8.5	2.2	7.5
Scatterometer ERS	9.4	2.4	8.3
Scatterometer Quickscat			8.2

In order to make a comparison mean wind speeds were recalculated from Quickscat and NCEP-NCAR for the period April 1999 to November 2002 since this is the data period presented for the observations in (Sommer 2003). This gives the same mean wind speed using NCEP-NCAR 7.5 m/s and a slightly higher wind speed using Quickscat of 8.4 m/s. This suggests using different data periods (shown in Table 6) does not substantially affect the results. The implication of this comparison is that both Quickscat and scatterometer from ARGOSS data appear to over-estimate the mean wind speed compared with the observations at Horns Rev although it is important to recall the following caveats:

- Areal averaging differs between the data sets
- The data period is not perfectly coincident
- The number of observations differs between the data sets, as does the accuracy and uncertainty of the data.
- The minimum detectable limit differs between the data sets, and treatment of data below sensor cut-in will potentially influence the robustness of the mean and the probability distribution.

Nevertheless, the apparent over estimation of the remotely sensed data is supported by comparison of scatterometer frequency distribution of wind speeds compared with Weibull fits from the observed data at 15 m and the NCEP-NCAR data which represent a height of 10 m (Figure 27). The scatterometer data gives a higher Weibull scale factor than either NCEP-NCAR or the observed data from 15 m. Similarly Figure 28 shows a comparison of the frequency distribution from altimeter and scatterometer also indicating higher wind speeds from the scatterometer. Figure 29 shows the cumulative probability distribution of wind speeds from the altimeter and NCEP-NCAR data sets showing relatively good agreement between these two datasets although as shown the altimeter data set is biased by the absence of measurements below approximately 1 m/s.

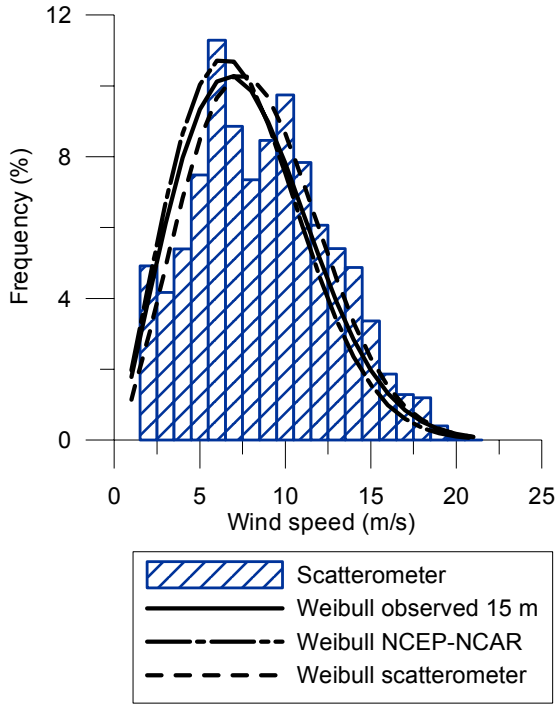

Figure 27. Comparison of wind speed frequency distribution from the different data sets.

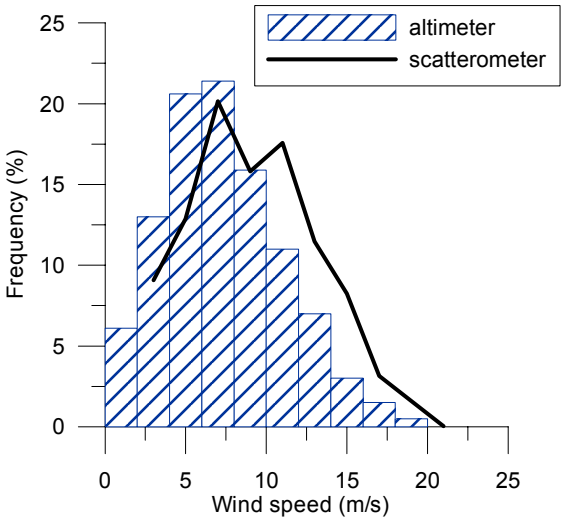

Figure 28. Comparison of wind speed frequency distribution from altimeter and ERS scatterometer datasets.

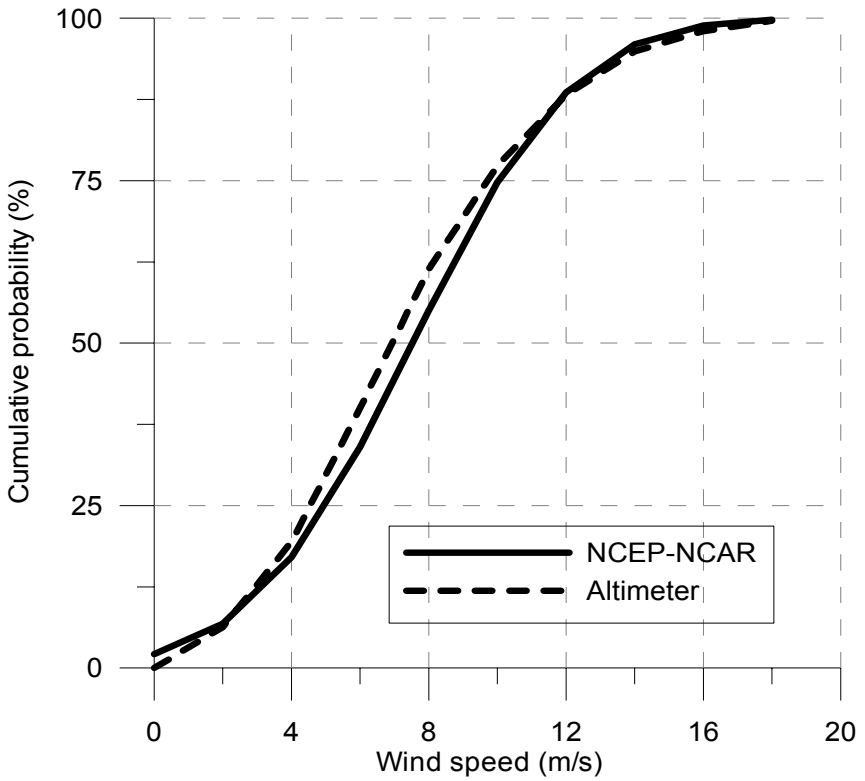

Figure 29. Comparison of cumulative probability distribution of wind speed from the altimeter and NCEP-NCAR data sets.

6.3.3 Diurnal wind variation versus satellite sampling time

Diurnal wind variations have not been considered. The recording time varies between satellite sensors. Altimeter winds are collected randomly in time as these satellites all are in non-sun-synchronous orbits. In contrast all other ocean surface wind observing satellites are in sun-synchronous orbits, e.g. morning/evening such as ERS and Envisat, or dawn/dusk such as QuikSCAT, see Appendix D for a list of sampling times. It may be advantageous to take benefit of combining the different types of satellite wind data as this: 1) increases the number of samples, and 2) diminishes the effect (bias) of diurnal variations for wind resource estimation based on satellite wind maps.

6.4 Concluding remarks

The comparison of different remotely sensed wind speeds with the NCEP-NCAR reanalysis data set and observations from the meteorological mast at Horns Rev indicate:

- The month-to-month variability of mean wind speeds appears to be larger in Quickscat and NCEP-NCAR than in the observations while altimeter data gives an even more pronounced seasonal cycle.
- Scatterometer (ERS) data from ARGOSS give a good representation of directional variability in comparison with the observations.
- The NCEP-NCAR reanalysis data appear to be more closely related to the in situ measurements than do the scatterometer data.

It is important to restate that comparisons of remotely sensed and in situ data are limited by a number of considerations:

- Comparison of point measurements from a meteorological mast with areally averaged observations from satellites and a reanalysis model may be biased due to spatial heterogeneity of flow regimes. Specific to this analysis, the above results may reflect some influence from the coastal zone.
- Variations in the data set density, and also differing levels of precision, minimum detectable limits and accuracy.
- Differences in the data periods and sampling times.

7 Wave heights

For the periods, 1st July 1999 to 23rd April 2000, 25th July to 30th November 2000, and 2nd January to 15th August 2003, the significant wave heights – average of the highest third of the waves – measured at the Horns Rev wind-turbine site south wave rider at position UTM zone 32, 426500 easting, 6149200 northing, (uncertainty 200 m), have been binned into 0.25 m height intervals on a monthly basis, and the percentages distribution calculated. This is shown in table 7, while the most significant – highest percentage – and the maximum wave heights found for the months are plotted in figure 30. With monthly basis is meant, that e.g. all July data go into the July column, no matter the year. Within the mentioned dataset periods there are several shorter periods without data, most of a few hours length, some of a day or two, two of one week and a one of two weeks.

The wave data are kindly provided by Elsam Engineering. Comparison to wave data from satellite observations is in progress.

Table 7 Monthly distribution - percentages - of significant wave heights for the total of the available dataset, which covers periods: 1st July 1999 to 23rd April 2000, 25th July to 30th November 2000, and 2nd January to 15th August 2003.

≥ m	< m	Jan	Feb	Mar	Apr	May	Jun	Jul	Aug	Sep	Oct	Nov	Dec
0.00	0.25	0.00	0.00	0.33	6.21	4.29	7.79	1.90	1.43	0.00	0.00	0.00	0.00
0.25	0.50	5.47	18.96	23.64	17.22	19.01	20.82	21.97	31.64	4.28	5.54	1.48	0.00
0.50	0.75	12.21	23.02	19.69	28.17	26.84	23.09	32.74	26.31	27.62	9.52	5.39	0.00
0.75	1.00	13.80	15.87	15.75	21.96	26.91	23.73	19.13	18.33	24.77	11.24	8.74	1.48
1.00	1.25	13.80	8.71	13.56	12.01	14.58	6.23	13.40	10.35	22.27	19.05	20.53	6.40
1.25	1.50	12.21	9.62	10.36	7.00	4.36	4.46	7.50	5.02	13.42	16.86	22.01	4.93
1.50	1.75	14.24	6.73	5.95	3.16	2.52	5.45	1.85	3.33	5.71	11.32	13.43	10.84
1.75	2.00	10.43	4.54	3.72	2.37	0.95	6.37	0.99	1.80	1.78	9.21	14.83	14.29
2.00	2.25	5.47	3.79	2.60	1.00	0.48	1.77	0.30	1.22	0.07	5.85	7.57	16.75
2.25	2.50	3.62	4.06	1.53	0.84	0.00	0.21	0.22	0.58	0.07	4.29	3.51	21.67
2.50	2.75	3.69	1.82	1.11	0.05	0.00	0.00	0.00	0.00	0.00	2.89	2.03	14.78
2.75	3.00	2.48	1.66	1.02	0.00	0.07	0.07	0.00	0.00	0.00	2.42	0.39	4.93
3.00	3.25	1.08	0.43	0.42	0.00	0.00	0.00	0.00	0.00	0.00	1.17	0.08	1.97
3.25	3.50	0.32	0.27	0.19	0.00	0.00	0.00	0.00	0.00	0.00	0.47	0.00	0.99
3.50	3.75	0.45	0.27	0.14	0.00	0.00	0.00	0.00	0.00	0.00	0.16	0.00	0.49
3.75	4.00	0.45	0.21	0.00	0.00	0.00	0.00	0.00	0.00	0.00	0.00	0.00	0.49
4.00	4.25	0.32	0.00	0.00	0.00	0.00	0.00	0.00	0.00	0.00	0.00	0.00	0.00
4.25	4.50	0.00	0.05	0.00	0.00	0.00	0.00	0.00	0.00	0.00	0.00	0.00	0.00
	Total	100	100	100	100	100	100	100	100	100	100	100	100
	Count	1573	1872	2153	1899	1468	1412	2321	1893	1401	1281	1281	203

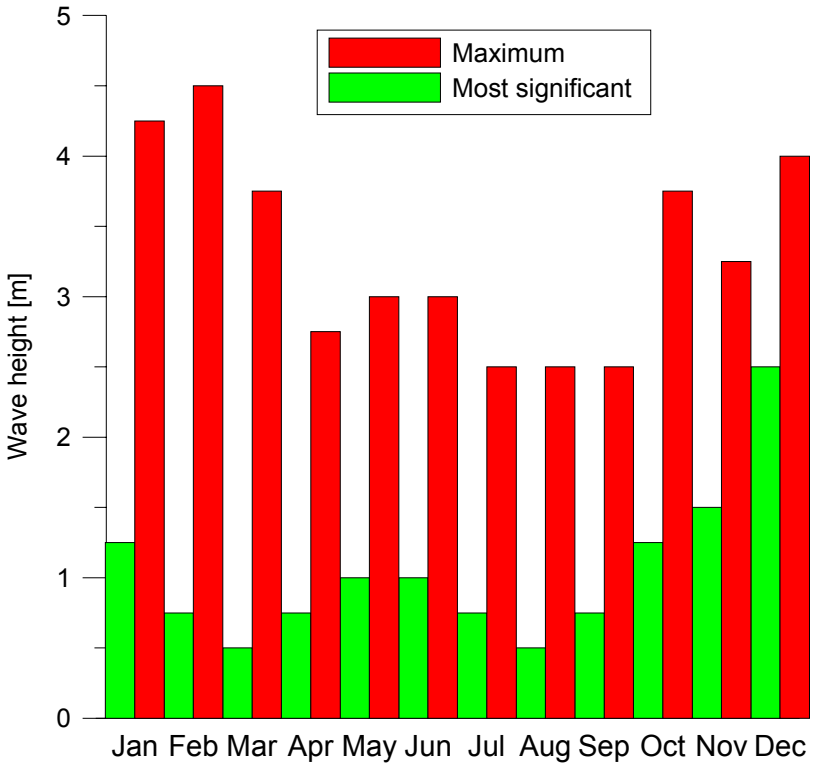

Figure 30: Monthly most significant and maximum measured wave heights.

8 Conclusion

Satellites map various parameters of interest for wind energy applications.

- Digital elevation model (DEM) from the Shuttle Radar Topography Mission (SRTM) seems adequate for wind resource modelling. Software for applied use is developed.
- Land cover types can be mapped from optical high-resolution satellite sensors such as Landsat TM. It is however necessary to find the relevant roughness length for each specific land cover type. This typically will be done during field visits. Also obstacle information (hedges, houses, groups of trees etc) will have to be identified in the field as these small-scale objects either are not seen in the satellite image, or are eliminate during the image processing to obtain a suitable spatial resolution for applied use in WASP.
- Surface wind vectors over the ocean can be obtained from Synthetic Aperture Radar (SAR) and scatterometer. Based on these wind observation software and service for applied use for wind resource assessment is developed. It is the observed wind climate (OWC) at 10 m above sea level that is obtained.

  Advantages of SAR wind maps are

  1. The wind resource map covers the coastal zone from 3 to 50 km offshore.
  2. A high spatial detail with 400 m by 400 m grid cells is available.
  3. SAR wind map processing time is around 2 weeks on pc for a skilled user incl. image order, processing and wind resource calculation, hence it is relatively fast.

  Advantages of scatterometer are

  4. A high number of wind maps from many sensors are available.
  5. On-line data from ERS scatterometer are available at ARGOSS.

The major limitation for both SAR and scatterometer satellite wind maps is the relatively low absolute accuracy, ~ 1.3 ms^{-1} and 20º rms. For scatterometer, the observed wind climate is from a location far offshore and modelling to the coastline will have to be done in WASP using topography and roughness information. For both data types modelling to hub-height is also necessary. WASP is recommended.

Ocean surface wind resource maps could be useful for pre-feasibility studies and in combination with offshore meteorological data. The satellite-based wind resource maps may be used to extrapolate to nearby sites and for screening larger regions for variation in the coastal offshore wind resource.

Acknowledgments

Funding for the EO-windfarm project from ESA EOMD 17736/03/I-IW for development of software for applied use of satellite information for wind energy application is gratefully acknowledged and collaboration with all partners is appreciated. Basic research funding is from the Danish Research Agency, Danish Technical Research Council (STVF) Sagsnr. 2058-03-0006 for the SAT-WIND project is also acknowledged. ERS SAR images are from the ESA AO-153 and EO-1356 projects. The images from EO-1356 are paid by EU-WEMSAR project, STVF SAR-WAKE project (Sagsnr. 26-02-0312) and STVF SAT-WIND project. QuikSCAT images are from CERSAT/IFREMER (Plouzane, France). Altimeter and scatterometer wind data are from ARGOSS, the Netherlands. CORINE map is from EEA. AIS map is from Danish National Environmental Research Institute. SRTM data are from JPL/NASA. Landsat images are from RS-model indlejring project (Danish Research Agency, indlejring) (Courtesy Eva Bøgh). Digital elevation map of a site in Spain is from VESTAS A/S. Meteorological observations are from Horns Rev from Elsam Engineering A/S. NCAR/NCEP re-analysis data from NOAA/NESDIS. Roughness map is from DK-wind resource project (Risø/EMD). WEMSARtool is from NERSC.

References

Astrup, P.; Larsen, S.E., *WAsP engineering flow model for wind over land and sea*. Risø-R-1107(EN) (1999) 20 p.

Barthelmie, R. J.; Pryor, S. C. (2003) Can satellite sampling of offshore wind speeds realistically represent wind speed distributions? *Journal of Applied Meteorology*, **42**, 83-94.

Christiansen, M.B. (2004): Wind energy studies offshore using satellite remote sensing. *Youth Symposium, World Energy Congress, Sydney, Australia*. Web published.

Christiansen, M.B.; Hasager, C.B., Detection of wind wakes offshore from satellite sar. In: Abstracts (CD-ROM). *35. COSPAR Scientific Assembly 2004*, Paris (FR), 18-25 Jul 2004. (CNES, Paris, 2004) 1 p

Cohen, A. C. (1965). Maximum-likelihood estimation in the Weibull distribution based on complete and on censored samples, *Technometrics*, **7**, 579–588.

Du, Y.; Vachon, P.W. and Wolfe, J. (2002), Wind direction estimation from SAR images of the ocean using wavelet analysis, *Canadian Journal of Remote Sensing*, **28,** 498.

European Environment Agency (1992), *CORINE land cover*, Commission of the European Communities, Directorate General XI, http://dataservice.eea.eu.int/dataservice/

Gash, J.H.C. (1986) A note on estimating the effect of a limited fetch on micrometeorological evaporation measurements, *Boundary-Layer Meteorology,* **35**, 409-413.

Gerling, T.W. (1986), Structure of the surface wind field from the SEASAT SAR, *Journal of Geophysical Research,* **91**, 2308.

Glazman, R. E. and A. Greysukh (1993). "Satellite altimeter measurements of surface winds." *Journal of Geophysical Research* **98**(C2): 2475-2483.

Guymer, T. H. and S. Zecchetto (1993). "Applications of scatterometer winds in coastal areas." *Internal Journal of Remote Sensing* **14**(9): 1787-1812

Harter, H. L. & Moore, A. H. (1968). Maximum-likelihood estimation from doubly censored samples of the parameters of the first asymptotic distribution of extreme values, *J. Am. Stats. Ass.*, 63, 889–901.

Hasager,CB, N W Nielsen, N O Jensen, E Boegh, J H Christensen, E Dellwik, H Soegaard, 2003, Effective roughness calculated from satellite-derived land cover maps and hedge-information used in a weather forecasting model. *Boundary-Layer Meteorology*, 109, p. 227-254.

Hasager,CB, R J Barthelmie, M B Christiansen, M Nielsen, S C Pryor. Quantifying offshore wind resources from satellite wind maps: study area the North Sea. 2004a. *Proceedings of the European Wind Energy and Exhibition Conference (EWEC) 2004*, 22-26 November 2004, London, UK.(to appear, 10p)

Hasager, C. B.; Dellwik, E.; Nielsen, M.; Furevik, B. (2004b) Validation of ERS-2 SAR offshore wind-speed maps in the North Sea. *International Journal of Remote Sensing*, **25**, 3817-3841.

Hasager,CB, M Nielsen, M B Christiansen. Quantitative remote sensing: Horns Rev wind farm case study. 2004c. SP-572 Envisat/ERS Symposium Proceedings, 6-10 September 2004, Salzburg, Austria.(to appear, 6p)

Hasager,CB, M Nielsen, M B Christiansen. RWT tool: offshore wind energy mapping from SAR. 2004d. *SP-572 Envisat/ERS Symposium Proceedings*, 6-10 September 2004, Salzburg, Austria. (to appear, 6p)

Hasager, C.B., Nielsen, M., Astrup, P, Barthelmie, R., Dellwik, E., Jensen, N.O., Jørgensen, B.H., Pryor, S.C., Rathmann, O., Furevik, B.R. 2004e Offshore wind resource estimation from satellite SAR wind field maps. *Wind Energy* (submitted)

Horst, T.W. and Weil, J.C. (1994) How far is far enough? - The fetch requirements for micrometeorological measurement of surface fluxes, *Journal of Atmospheric and Oceanic Technology,* **11**, 1018-1025.

Kalnay, E., M. Kanamitsu, et al. (1996). "The NCEP/NCAR 40-year Reanalysis Project." *Bulletin of the American Meteorological Society* **77**(3): 437-470

Kistler, R., E. Kalnay, et al. (2001). "The NCEP-NCAR 50 year reanalysis: Monthly mean CD-ROM and documentation." *Bulletin of the American Meteorological Society* **82**: 247-267

Lenschow, D. H., Mann, J. & Kristensen, L. (1994). How long is long enough when measuring uxes and other turbulence statistics, *J. Atmos. Ocean. Technol.*, 11, 661–673.

Lillesand,TM, R W Kiefer, 1987, *Remote sensing and image interpretation*, New York, John Wiley & Sons, p. 1-721.

Monaldo,F, V Kerbaol, P Clemente-Colón, B Furevik, J Horstmann, J Johannessen, X Li, W Pichel, T D Sikora, D J Thomson, C Wackerman. The SAR measurement of ocean surface winds:an overview. ESA SP-565, 15-32. 2003. *ESA. Proceedings of the Second Workshop Coastal and Marine Applications of SAR*, 2-12 September 2003, Svalbard, Norway.

Mortensen, N. G.; Landberg, L.; Rathmann, O. ; Nielsen, M.; Nielsen, P. (1999), A detailed and verified wind resource atlas for Denmark, *In: Wind engineering into the 21. century. International conference on wind engineering (10. ICWE),Copenhagen (DK), 21-24 Jun 1999.,* Eds.: A. Larsen, G. L. Larose and F. M. Livesey, A. A. Balkema, Rotterdam, **3.10***,* 2013-2018.

National Environmental Research Institute (2001), *AIS - The Danish Areal Information System,* http://www.dmu.dk/1_viden/2_miljoe-tilstand/3_samfund/ais/index_en.htm

Press, W. H., Flannery, B. P., Teukolsky, S. A. & Vetterling, W. T. (1992). *Numerical Recipes in C, second edition*, Cambridge University Press.

Pryor, S. C.; Nielsen, M.; Barthelmie, R. J.; Mann, J. (2004) Can satellite sampling of offshore wind speeds realistically represent wind speed distributions? Part II Quantifying uncertainties associated with sampling strategy and distribution fitting methods. *Journal of Applied Meteorology*, **43**, 739-750.

Pryor, S. C. and R. J. Barthelmie (2002). "Statistical analysis of flow characteristics in the coastal zone." *Journal of Wind Engineering and Industrial Aerodynamics* **90**: 201-221

Sommer,A. Offshore measurements of wind and waves at Horns Rev and Laesoe, Denmark. 65-79. 2003. *Proceedings of the Offshore Wind Energy of the Mediterranean Seas and other Seas (OWEMES)* 10-12 April 2003, Naples, Italy. Athena. ATHENA/ENEA

Stoffelen, A. and Anderson, D.L.T. (1997), Scatterometer data interpretation: Estimation and validation of the transfer function CMOD4, *Journal of Geophysical Research,* **102**, 5767.

Tournadre, J. and R. Ezraty (1990). "Local climatology of wind and sea state by means of satellite radar altimeter." *Journal of Geophysical Research* **Oceans, 95**(C10): 18255-18268

van Hulle,F, S le Bot, V van Lancker, S Deleu, J P Henriet, Y Cabooter, G Palmers, L Dewilde, J Soens, J Driesen, van Roy, P, R Belmans. *Optimal offshore wind energy developments in Belgium.* 1-153. 2004. Brussels, Belgian Science Policy. Scientific Support Plan for a Sustainable Development Policy (SPSD II).

Wentz,FJ. A well calibrated ocean algorithm for SSM/I. 101395, 1-34. 1995. Santa Rosa, CA, Remote Sensing Systems. *RSS Tech. Report 101395*.

Appendix A List of acronyms

ADEOS	Advanced Earth Observations Satellite (of NASDA)
AFRL	Air Force Research Laboratory, USA
AIS	Danish Areal Information System
AMI	Active Microwave Instrument (of ESA)
AMSR-E	Advance Microwave Scanning Radiometer (of NASA)
APP	Alternating Polarization Precision
Aqua	Satellite platform (of NASA)
ARGOSS	Company in the Netherlands
ASAR	Advanced Synthetic Aperture Radar (of ESA)
AVHRR	Advanced Very High Resolution Radiometer (of NOAA)
C-band	microwave wavelength ~5.3 cm
CERSAT	Centre ERS d'Archivage et de Traitement - *French facility*
CMOD	C-band geophysical model function
CNES	Centre National d'Etudes Spatiales (French Space Agency)
CORINE	Name of programme that developed the CORINE land cover map
CSA	Canadian Space Agency
DEM	Digital elevation model
DESCW	Display Earth remote sensing Swath Coverage for Windows (of ESA)
DMPS	Defence Meteorological Satellite Program (USA)
EEA	European Environmental Agency
EMD	Energi- og MiljøData, company in Denmark
Envisat	European Environmental Satellite (of ESA)
EOLI	Earthnet OnLine Interactive (web system at ESA for image catalogue)
EOMD	Earth Observation Market Development (of ESA)
EO-windfarm	Earth Observation wind farm project (http://www.org-eowindfarm.org)
ERS	European Remote Sensing satellite (of ESA)
ESA	European Space Agency
FFT	Fast Fourier Transform
GEOSAT	Geodetic Satellite altimeter (of US Navy)
GFO	Geosat Follow-on radar altimeter (of US Navy)
GMT	Greenwich Mean Time
IKONOS	Satellite and instrument name (of Space Imaging)
IMG	Image mode of Envisat ASAR imagery
IRS-1C	Indian Remote Sensing Satellite (of National Remote Sensing Agency)
Jason	Satellite platform (of NASA and CNES)
JAXA	Japan Aerospace Exploration Agency
JPL	Jet Propulsion Laboratory, USA
Landsat	Land (Remote Sensing) Satellite and sensor (of NASA)
LISS-III	Linear Imaging Self-Scanning Sensor (of India)
MERIS	MEdium Resolution Imaging Spectrometer Instrument (of ESA)
Midori	Japanese for 'green', a satellite platform (of NASDA)
ML	maximum-likelihood
MODIS	MEdium Resolution Imaging Spectrometer Instrument (of NASA)
NASA	National Aeronautics and Space Administration
NASDA	National Space Development Agency of Japan (now JAXA)
NCAR	National Center for Atmospheric Research, USA
NCEP	National Centers for Environmental Prediction, USA
NERSC	Nansen Environmental and Remote Sensing Center, Norway
NESDIS	National Environmental Satellite, Data, and Information Service, USA
NLCD	National Land Cover Data, USA
NOAA	National Oceanic & Atmospheric Administration, USA
NRL	Naval Research Laboratory, USA
NSCAT	NASA Scatterometer
Poseidon	Radar altimeter (of CNES)
QuickBird	Satellite platform and sensor (of DigitalGlobe)

QuikSCAT	Quick Scatterometer satellite platform (of NASA)
RA	Radar altimeter (of ESA)
Radarsat	Radar satellite platform and sensor (of CSA)
RWT	Risø WEMSAR Tool (software) (of Risø)
SAR	Synthetic Aperture Radar
SAR-WAKE	Offshore wake effect study from Earth Observation Synthetic Aperture Radar (project of Risø/STVF)
SAT-WIND	Winds from satellites for offshore and coastal wind energy mapping and wind-indexing research project (project of Risø/STVF)
SeaWIFS	Sea-viewing Wide Field-of-view Sensor (of NASA)
SeaWinds	Scatterometer instrument (on QuikSCAT of NASA)
SPOT	Systeme pour l'Observation de la Terre (French satellite sensor of CNES)
SRTM	Shuttle Radar Topography Mission (of NASA)
SSM/I	Special Sensor Microwave/Image (of US Department of Defense)
STVF	Statens Teknisk Videnskabelig Forskningsråd (Danish Technical Research Council)
Terra	Satellite platform (of NASA)
TOPEX	Radar altimeter (of NASA)
UTC	Coordinated Time Universal
UTM	Universal Transverse Mercator Coordinate system
WASP	Wind Atlas and Analysis Program (of Risø)
WEMSAR	Wind Energy Mapping using Synthetic Aperture Radar project
WEMSARtool	Wind Energ Mapping using SAR tool (software) (of NERSC)
WGS84	World Geodetic System 1984
WSM	Wide Scan Mode

Appendix B Examples of wind maps

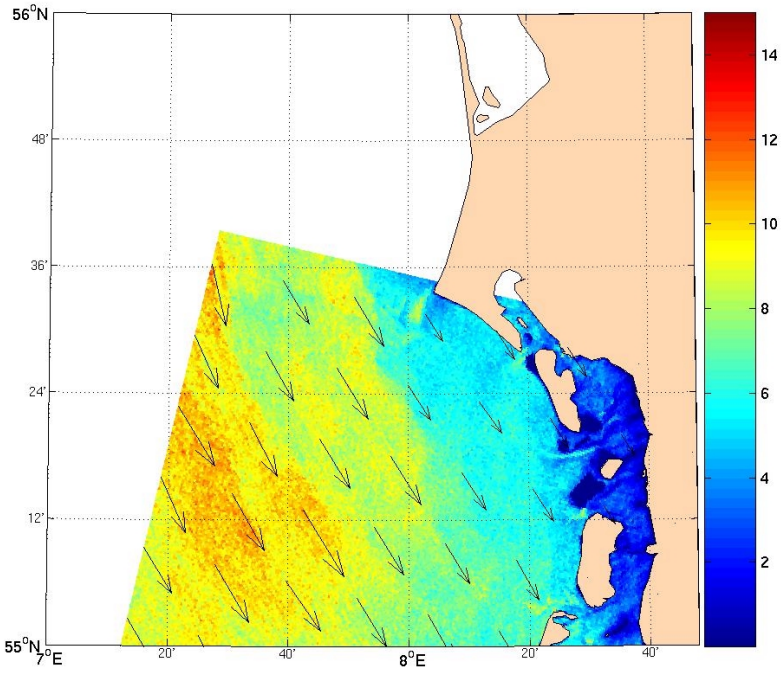

Figure 31: ERS-2 SAR wind map is from Horns Rev in the North Sea, 10 August 1999. The arrows indicate wind direction and the colour scale wind speed in ms^{-1}. CMOD4 is used to calculate wind speed. Each wind grid cell is 400 m by 400 m. The image covers 100 km by 100 km. Courtesy Birgitte Furevik, NERSC.

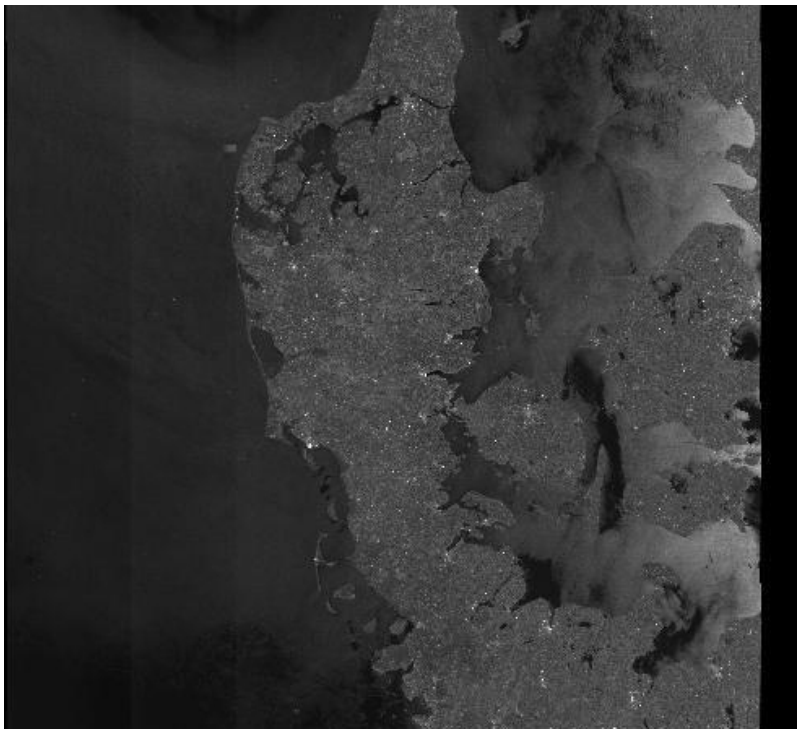

Figure 32: Envisat ASAR Wide Scan Mode image is from Denmark, 28 July 2004. The images is from ESA EOLI web-server. It is raw data in quicklook format. Each wind grid cell will be around 2.5 km by 2.5 km. The image covers 405 km by 405 km.

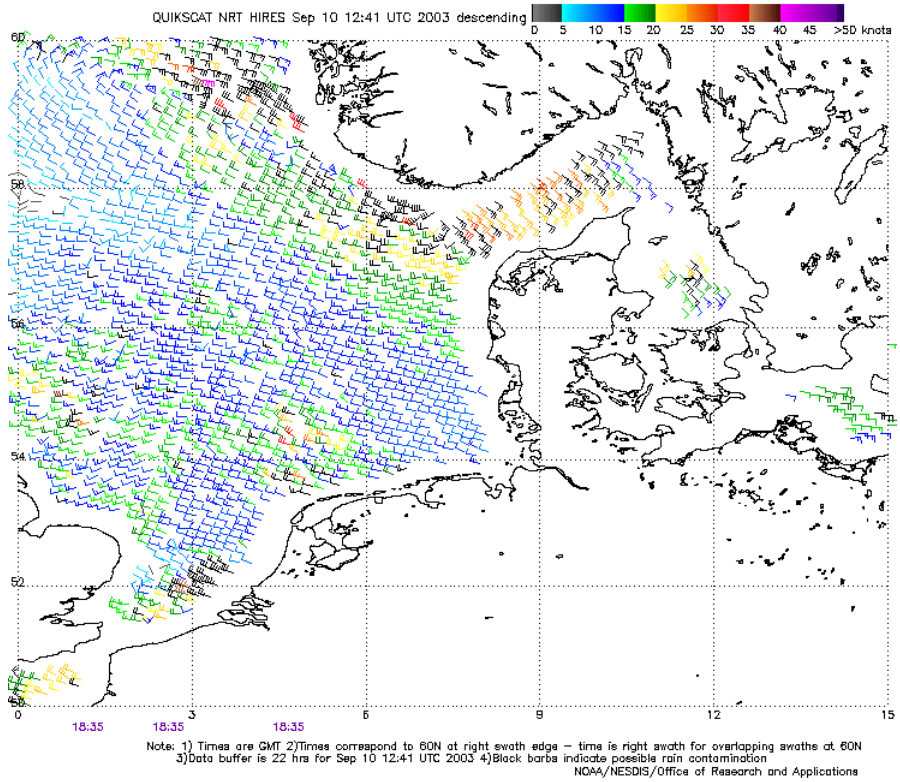

Figure 33: QuikSCAT wind map is from the North Sea and Denmark, 10 September 2003. The arrows indicate wind direction and the colour scale wind speed in knots. The image is from NOAA/NESDIS web server. Each wind grid cell is 25 km by 25 km. The swath is 1800 km so only part of the swath is shown in this figure.

The swath is the field of view across-track for a given satellite sensor. For ERS SAR the swath is 100 km, for Envisat ASAR Wide Scan Mode 405 km and for QuikSCAT 1800 km. These satellites all are in polar orbits. It means that the temporal coverage is better at higher latitude than it is at the Equator.

Appendix C Satellite wind products

Table 8. Satellite ocean surface winds data products. Acronyms in Appendix A

.

	Period	Coverage Swath (km)	Wind cell (km)	Repeat time	Accuracy	Wind data type	Data owner
Scatterometer							
ERS-1 AMI	1991-1996	500	25	3 days	1.30*	wind vector	ESA
ERS-2 AMI	1995-2001	500	25	3 days	1.20*	wind vector	ESA
ADEOS-1 NSCAT	1996-1997	600	25	1per day	<2.0** 20º	wind vector	NASA
QuikSCAT SeaWinds	1999-now	1800	25	2 per day	<2.0** 20º	wind vector	NASA
Midori-2 SeaWinds	2003-now	1800	25	2 per day	<2.0** 20º	wind vector	NASA/ NASDA
SAR							
ERS-1 SAR	1991-1996	100	0.4	10 days	&	wind vector	ESA
ERS-2 SAR	1995-now	100	0.4	10 days	&	wind vector	ESA
Envisat ASAR (IMG and APP)	2002-now	100	0.4	10 days	&	wind vector	ESA
Envisat ASAR (WSM)	2002-now	405	2.5	3 days	&	wind vector	ESA
Radarsat (standard)	1995-now	45	0.4	12 days	&	wind vector	CSA
Radarsat (scanmode)	1995-now	500	2.5	3 days	&	wind vector	CSA
Altimeter							
Geosat	1985-1989	25	25	17 days	2.47*	wind speed	US Navy
ERS-1 RA	1991-1996	25	25	35 days	1.59*	wind speed	ESA
ERS-2 RA	1996-now	25	25	35 days	1.56*	wind speed	ESA
Topex	1992-now	25	25	10 days	1.59*	wind speed	NASA/ CNES
Poseidon	1992-now	25	25	10 days	1.70*	wind speed	NASA/ CNES
GFO	1998-now	25	25	17 days	1.43*	wind speed	US Navy
Jason-1	2002-now	25	25	10 days	1.34*	wind speed	NASA/ CNES
Passive microwave							
DMSP SSM/I	1987-now	1400	25	~6 per day	0.9§	wind speed	NASA/ DMPS
Aqua AMSR-E	2002-now	1445	24	~2 per day	1.5¤	wind speed	NASA /NASDA
Coriolis/WindSat	2003-now	1000	25	1 per day	2.0# 20º	wind vector	NRL/ AFRL

* Standard error in raw images in ms^{-1} for 2-24 ms^{-1} (Source:ARGOSS http://www.waveclimate.com/)
** Nominal values for mean wind speed and wind direction for wind speed range 2-24 ms^{-1}
& CMOD algorithms < 2ms^{-1}, 20º for 2-24 ms^{-1}
§ 0.9 ms^{-1} for 0-20 ms^{-1} (Wentz, 1995)
¤ Nominal values for mean wind for range 3-25 m s^{-1}
Nominal values for mean wind speed and direction for wind speed range 3-25 ms^{-1}

In the present study satellite data are used as follows:

Altimeter ERS-1/-2, Topex, Poseidon, Jason-1 and GFO: ARGOSS http://www.argoss.nl/

Scatterometer ERS-1/-2 data: ARGOSS http://www.argoss.nl/

Scatterometer QuikSCAT: CERSAT http://www.ifremer.fr/cersat/en/welcome.htm

SAR from ERS-1/-2 and Envisat: ESA http://pooh.esrin.esa.it/services/catalogues.html

Appendix D Satellite sampling times

Table 9: Equatorial crossing times in Local Standard Time (local time zone).

Platform	Instrument	Ascending	Descending
QuikBird	QuikSCAT	05:51	17:51
Envisat	ASAR	10.00	21.00
ERS-1/-2	AMI (SAR & SCAT)	10.30	21.30
Aqua	AMSR-E	13:30	01:30
Radarsat-1	SAR	18.00	06.00
Coriolis	WindSat	18.00	06.00
DMSP F13	SSM/I	18:15	06:15
DMSP F14	SSM/I	20:21	08:21
ADEOS-1	NSCAT	21.30	10.30
DMSP F15	SSM/I	21:31	09:31
Midori-II	SeaWinds	22:30	10:30

Ascending and descending are northbound and southbound modes, respectively.

Appendix E
Maximum-likelihood probability estimation by censored data

Wind speeds estimates by SAR images rely on a statistical correlation valid in a specified range of wind speeds $[u_1 \ldots u_2]$. Images are often expensive and since detailed analysis involves considerable manual work, the user is tempted to purchase only a subset of the available images. The image provider has often made preliminary analyses and prepared a catalogue guiding the user to relevant data.

Table 10 gives an account of the data. The out-of-range data are generally not purchased, but from the catalogue the user know the numbers n_1 below the lower threshold u_1, and n_2 above the upper threshold u_2 . Depending on project resources the user analyses n and disregard n_0 of the valid scenes. There may be other reasons to reject an image, e.g. if it contains false readings in the area of interest or a large fraction of the footprint is outside the image. The rejected data are, however, not included in the categories listed in Table 10.

Table 10. Data counting

wind speed $< u_1$ (n_1 scenes)	unused in-range data (n_0 scenes)	wind speed $> u_2$ (n_2 scenes)
	analysed in-range data (n scenes)	

ML estimates

The maximum-likelihood method may be extended to provide an unbiased estimate of the real distribution by censored data. Following Harter & Moore (1968) we derive an extended maximum-likelihood function, which account for the added information in Table 10.

$$L(A,k) = \frac{(n+n_0+n_1+n_2)!}{n_0!\,n_1!\,n_2!} F(u_1|A,k)^{n_1}\,[1-F(u_2|A,k)]^{n_2} \\ [F(u_2|A,k)-F(u_1|A,k)]^{n_0} \prod_{i=1}^{n} p(u_i|A,k) \quad \text{(E.10)}$$

The conventional model for wind speed is the two-parameter Weibull probability distribution $F(u) = 1 - \exp\left[-(u/A)^k\right]$ and corresponding probability density function is $p(u) = dF/du$. With insertion of this distribution and the short-hand notation $s_i = u_i/A$, $s_1 = u_1/A$ and $s_2 = u_2/A$, the logarithm of the maximum-likelihood function becomes:

$$\ln L(k,A) = n\ln k - n\ln A + (k-1)\sum_{i=1}^{n}\ln s_i - \sum_{i=1}^{n} s_i^k \\ + n_0 \ln\left[\mathrm{e}^{-s_1^k} - \mathrm{e}^{-s_2^k}\right] + n_1 \ln\left[1-\mathrm{e}^{-s_1^k}\right] - n_2 s_2^k + \text{const.} \quad \text{(E.11)}$$

This function generally has a single maximum at a point, which defines the ML estimates $\hat{A}$ and $\hat{k}$ and may be found numerically. Powells' minimization method (Press, Flannery, Teukolsky & Vetterling 1992) usually takes three iterations in the outer loop to determine A and k with four-decimal accuracy.

Uncertainty of ML estimates

The distribution of ML estimates is asymptotically Gaussian and the expected covariance matrix of these is (Cohen 1965, e.g.):

$$\begin{bmatrix} \mathrm{Var}(\hat{A}) & \mathrm{Cov}(\hat{A},\hat{k}) \\ \mathrm{Cov}(\hat{A},\hat{k}) & \mathrm{Var}(\hat{k}) \end{bmatrix} = \begin{bmatrix} -\frac{\partial^2 \ln L}{\partial A^2}\Big|_{\hat{A},\hat{k}} & -\frac{\partial^2 \ln L}{\partial A \partial k}\Big|_{\hat{A},\hat{k}} \\ -\frac{\partial^2 \ln L}{\partial A \partial k}\Big|_{\hat{A},\hat{k}} & -\frac{\partial^2 \ln L}{\partial k^2}\Big|_{\hat{A},\hat{k}} \end{bmatrix}^{-1} \tag{E.12}$$

The second-order derivatives of the ML function E.10 are

$$\begin{aligned}
\frac{\partial^2 \ln L(k,A)}{\partial A^2} &= \frac{k}{A^2}\left[n - (1+k)\sum_{i=1}^{n} s_i^k \right. \\
&- n_0 \left(\frac{(1+k)\left(s_1^k \mathrm{e}^{-s_1^k} - s_2^k \mathrm{e}^{-s_2^k}\right)}{\mathrm{e}^{-s_1^k} - \mathrm{e}^{-s_2^k}} + \frac{k \mathrm{e}^{-s_1^k - s_2^k}\left(s_2^k - s_1^k\right)^2}{\left(\mathrm{e}^{-s_1^k} - \mathrm{e}^{-s_2^k}\right)^2} \right) \\
&\left. + n_1 \left(\frac{1+k}{1-\mathrm{e}^{-s_1^k}} - \frac{k s_1^k}{\left(1-\mathrm{e}^{-s_1^k}\right)^2} \right) s_1^k \mathrm{e}^{-s_1^k} - n_2 (1+k) s_2^k \right] \\
\frac{\partial^2 \ln L(k,A)}{\partial A \partial k} &= \frac{1}{A}\left[-n + \sum_{i=1}^{n} s_i^k + k \sum_{i=1}^{n} s_i^k \ln s_i \right. \\
&+ n_0 \left(\frac{s_1^k \mathrm{e}^{-s_1^k}(1 + k \ln s_1) - s_2^k \mathrm{e}^{-s_2^k}(1 + k \ln s_2)}{\mathrm{e}^{-s_1^k} - \mathrm{e}^{-s_2^k}} \right. \\
&\left. + \frac{k \mathrm{e}^{-s_1^k - s_2^k}(s_1^k - s_2^k)(s_1^k \ln s_1 - s_2^k \ln s_2)}{\left(\mathrm{e}^{-s_1^k} - \mathrm{e}^{-s_2^k}\right)^2} \right) \\
&\left. - n_1 \left(\frac{1 + k \ln s_1}{1-\mathrm{e}^{-s_1^k}} - \frac{k s_1^k \ln s_1}{\left(1-\mathrm{e}^{-s_1^k}\right)^2} \right) s_1^k \mathrm{e}^{-s_1^k} + n_2 \left(1 + k \ln s_2\right) s_2^k \right] \\
\frac{\partial^2 \ln L(k,A)}{\partial k^2} &= -\frac{n}{k^2} - \sum_{i=1}^{n} s_i^k (\ln s_i)^2 \\
&- n_0 \left(\frac{s_1^k \mathrm{e}^{-s_1^k} (\ln s_1)^2 - s_2^k \mathrm{e}^{-s_2^k} (\ln s_2)^2}{\mathrm{e}^{-s_1^k} - \mathrm{e}^{-s_2^k}} + \frac{\mathrm{e}^{-s_1^k - s_2^k}(s_1^k \ln s_1 - s_2^k \ln s_2)^2}{\left(\mathrm{e}^{-s_1^k} - \mathrm{e}^{-s_2^k}\right)^2} \right) \\
&+ n_1 \left(\frac{1}{1-\mathrm{e}^{-s_1^k}} - \frac{s_1^k}{\left(1-\mathrm{e}^{-s_1^k}\right)^2} \right) s_1^k \mathrm{e}^{-s_1^k} (\ln s_1)^2 - n_2 s_2^k (\ln s_2)^2
\end{aligned} \tag{E.13}$$

Moment statistics

The n-order statistical moment of a stochastic variable with Weibull distribution is

$$\langle u^n \rangle = m_n = A^n \Gamma\left(1 + n/k\right) \tag{E.14}$$

and its normalized derivative is

$$\frac{dm_n}{m_n} = \frac{n\, dA}{A} - \frac{n}{k^2} \psi\left(1 + n/k\right) dk \tag{E.15}$$

where $\psi(x)$ is the digamma function, i.e. the normalized derivative of the Gamma function $\Gamma'(x)/\Gamma'(x)$. Thus, the uncertainty of statistical moment is linked to the covariance matrix of the ML estimates.

$$\frac{\sigma_{m_n}^2}{m_n^2} = n^2 \left[\frac{\sigma_A^2}{A^2} + \psi^2\left(1 + n/k\right) \frac{\sigma_k^2}{k^4} - 2\psi\left(1 + n/k\right) \frac{\mathrm{Cov}(A,k)}{A\, k^2} \right] \tag{E.16}$$

and

$$\frac{\mathrm{Cov}(m_n, m_p)}{m_n m_p} = np \left[\frac{\sigma_A^2}{A^2} + \psi\left(1 + n/k\right) \psi\left(1 + p/k\right) \frac{\sigma_k^2}{k^4} \right.$$
$$\left. - \left[\psi\left(1 + n/k\right) + \psi\left(1 + p/k\right)\right] \frac{\mathrm{Cov}(A, k)}{A\, k^2} \right] \quad \text{(E.17)}$$

From this we derive uncertainty of related statistics, e.g. the estimates of the central moment $\mu_2 = \langle (u - \mu)^2 \rangle = m_2 - m_1^2$ has the error variance $\sigma_{\mu_2}^2 = \sigma_{m_2}^2 + 4m_1^2\sigma_{m_1}^2 - 4m_1 \mathrm{Cov}(m_1, m_2)$ (Lenschow, Mann & Kristensen 1994) in which the terms are know by ML estimates.

Mission

To promote an innovative and environmentally sustainable technological development within the areas of energy, industrial technology and bioproduction through research, innovation and advisory services.

Vision

Risø's research **shall extend the boundaries** for the understanding of nature's processes and interactions right down to the molecular nanoscale.

The results obtained shall **set new trends** for the development of sustainable technologies within the fields of energy, industrial technology and biotechnology.

The efforts made **shall benefit** Danish society and lead to the development of new multi-billion industries.